Final Technical Report

Project Title:	High Performance Perovskite-Based Solar Cells
Project Period:	09/30/2014 – 10/31/2019 (includes 1 yr NCE)
Project Budget:	$1,300,002
Submission Date:	08/02/2019
Recipient:	Duke University
Address:	Duke University Office of Sponsored Programs 220 West Main Street, Suite 300 Durham, NC 27705-4677
Award Number:	DE-EE0006712
Project Team:	Duke University (lead) / University of Toledo (partner)
Contacts:	David Mitzi Professor Phone: 919-660-5356 Email: david.mitzi@duke.edu

Acknowledgment: "The information, data, or work presented herein was funded in part by the Office of Energy Efficiency and Renewable Energy (EERE), U.S. Department of Energy, under Award Number DE-EE0006712."

Disclaimer: "The information, data, or work presented herein was funded in part by an agency of the United States Government. Neither the United States Government nor any agency thereof, nor any of their employees, makes any warranty, express or implied, or assumes any legal liability or responsibility for the accuracy, completeness, or usefulness of any information, apparatus, product, or process disclosed, or represents that its use would not infringe privately owned rights. Reference herein to any specific commercial product, process, or service by trade name, trademark, manufacturer, or otherwise does not necessarily constitute or imply its endorsement, recommendation, or favoring by the United States Government or any agency thereof. The views and opinions of authors expressed herein do not necessarily state or reflect those of the United States Government or any agency thereof."

Executive Summary: Hybrid lead-halide perovskite semiconductors have become one of the most heavily studied photovoltaic (PV) materials within the past ten years. However, these materials suffer from two key limitations that have ultimately limited the progression towards commercialization: (i) the inclusion of toxic lead (Pb) and (ii) instability towards moisture, oxygen, and temperature. This project has targeted the development of perovskite absorber materials that replace Pb with a benign alternative and are stable under atmospheric conditions.

Under this wide goal, the project had four major objectives as detailed below:

1. Develop high-performance Pb-based PV devices and study alternative inorganic contact materials to improve the device stability;
2. Advance computational techniques to understand the electronic and optical properties of perovskite semiconductors from a theoretical perspective;
3. Explore various hybrid and inorganic halide, chalcohalide and chalcogenide perovskite absorbers as highly stable, Pb-free absorber alternatives;
4. Develop thin-film deposition and device fabrication methodologies to deposit high-quality Pb-free perovskite absorbers and high-performance devices.

Within the first objective, the researchers fabricated high-performing methylammonium lead iodide solar cells based on both traditional architectures (using a TiO_2 contact) and inverted architectures using NiO_x and novel $CuCrO_2$ as hole transport layers (HTL). The work with $CuCrO_2$ is the first work demonstrating $CuCrO_2$ as a promising contact material for future, stable perovskite solar cells. Towards the second objective researchers have calculated the intrinsic stability and optoelectronic properties of multiple Pb-free systems including chalcohalide (e.g. $CsBiOF_2$), halide (e.g. $Cs_3Sb_2I_9$), and chalcogenide perovskites (e.g. $BaZr_{1-x}Ti_xS_3$). Additionally, the researchers have furthered the basic understanding of perovskite materials by introducing the concept of electronic dimensionality and its impact on optoelectronic properties. This understanding has had implications in PV applications and beyond. In the third and fourth objectives, the investigators have exhausted a myriad of Pb-free materials in search of a stable, promising Pb-free perovskite absorber, including chalochalides based on $CsBiOF_2$, Pb-free halides (such as $Cs_2AgBiBr_6$, Cs_2TiBr_6, and $Cs(Ge/Sn)I_3$) , chalcogenide perovskites (e.g. $BaZrS_3$), and perovskite-related halides InI and silver bismuth iodide. While the researchers have studied many promising perovskites and perovskite-alternatives, a stable, high-performing Pb-free absorber has proven to be elusive.

In summary, through a combined theoretical and experimental strategy, a thorough understanding of Pb-based and Pb-free perovskite absorbers and state-of-the-art thin-film deposition and device fabrication strategies have been developed within this project.

Table of Contents

Background 3
Introduction 5
Project Results and Discussion 8
Conclusions 47
Budget and Schedule 47
Path Forward 48
Publications Resulting from This Work (referred as letters) 48
References (referred as numbers) 50

Background: Current solar cell technologies based on lead-halide perovskites have multiple advantages over other thin-film materials, particularly (i) very high absorption coefficient, (ii) low formation energy (readily forming) defects lie near the band edges, (iii) small carrier effective masses and high mobilities, (iv) relatively benign grain boundaries, and (v) simple thin-film processing by solution and vacuum-based techniques.[1] This combination of promising properties has led to outstanding device power conversion efficiencies (PCE) being reported in a relatively short development period—i.e. PCE values have increased from below 5% to above 25% in roughly ten years.[2] However, even with these intriguing properties, the highest performing perovskites depend on the unique properties of the toxic heavy metal lead (Pb) to achieve the high performance and tend to degrade when exposed to atmospheric conditions. The need to replace lead with a less toxic alternative and to improve the stability of the perovskite materials has driven much of the research within this project and within the wider research community.

In the pursuit of stable, Pb-free perovskite absorbers, multiple avenues have been taken including direct replacement of Pb with isoelectronic elements, replacing Pb with two or more cations to create double perovskites, and moving towards non-halide perovskites.

Direct replacement of Pb has been focused on developing perovskite materials based on Sn, Bi, and Sb, as was done in this project. The most successful strategies for fabricating Pb-free perovskite solar cells involve the replacement of Pb by Sn in conventional 3D hybrid perovskites such as $MAPbI_3$ or $FAPbI_3$. The highest efficiency of a totally non-Pb perovskite solar cell has reached 9%, using a predominantly $FASnI_3$ absorber, augmented by SnF_2 (to reduce Sn oxidation) and phenethylammonium iodide (PEAI), to improve film crystallinity and form protective deposits of 2-D perovskite phases).[3] Despite this success, the low photoluminescence lifetimes (<10 ns) of these films as well as low operational stability indicate that material defects still present a significant challenge to devices using Sn-based absorbers. Another intriguing material, and one that has been pursued in this project as well, is another true perovskite, $CsSn_{0.5}Ge_{0.5}I_3$.[4] The authors observe not only that devices with stabilized efficiency over 7% may be prepared, but that this level of performance can be sustained under continuous operation for ~500 h; moreover, the phase stability of this material as measured by XRD outstrips that of $CsSnI_3$, $CsPbI_3$, and $MAPbI_3$ under 1 sun light-soaking at 45 °C and 80% relative humidity. This surprising result is attributed to the observation that Ge addition stimulates

the formation of an amorphous germanium oxide crust on the surface of the perovskite film; this crust is in turn stabilized by a small (<10 at%) contribution of Sn to the metal content in the protective oxide. The oxide crust prevents further ingress of harmful species and may also electronically passivate the top interface. The strategy of directly replacing Pb by Sn is and will be a continuing source of promising Pb-free perovskite absorbers.

Alternatively, bismuth (Bi) and antimony (Sb)-based halide perovskites with the chemical structure $A_3(Bi/Sb)_2I_9$ (A= CH_3NH_3, Rb, Cs) are promising candidates to be utilized in solar cells, due to their superior air-stability compared to Pb-containing perovskite materials. Although some fundamental research has been done to study their crystal structures, a limited number of attempts have been done to utilize them for constructing solar cells. The highest reported efficiencies for $(CH_3NH_3)_3Bi_2I_9$, $Rb_3Bi_2I_9$ and $Cs_3Bi_2I_9$ are 0.39%,[5] 0.66%[6] and 1.09%,[7] respectively, demonstrating the demand for more research in this area. Similar levels of performance have been obtained for the antimony-based defect perovskite $(MA)_3Sb_2Cl_xI_{9-x}$, the layered phase of which may be stabilized relative to the dimer phase through the addition of the chloride.[8] In this vein, the current project investigated $Cs_3Sb_2I_9$, $Rb_3Bi_2I_9$ and $Cs_3Bi_2I_9$ from a thin-film deposition point of view, albeit with very limited success in fabricating high-performance solar cells.[A,W] Among different strategies to ameliorate the efficiency of these cells, alloying may be a promising way to modify the band gap of these materials to a more appropriate value for PV applications.

When replacing Pb with two (or more) elements, the only true perovskite to have demonstrated significant power conversion efficiency is the bismuth-based double perovskite $Cs_2AgBiBr_6$. Solar cells fabricated using this material as the absorber in a conventional mesoporous device architecture have reached 2.4% PCE under slow reverse J-V scan, and ~2% stabilized PCE, with good resilience during operation under ambient conditions.[9] However, the band gap of this material is rather high for use in a single junction solar cell (~2.2 eV) as well as being indirect. Consequently, the spectroscopically limited maximum efficiency (SLME) of this material is <8%, limiting its potential for future applications. Various other efforts have been made towards investigating halide double perovskites for PV applications (including in this project[I,L-P,R]) without as much success as $Cs_2AgBiBr_6$.[10]

Outside of halide perovskites, two classes of materials, mixed chalcohalide and chalcogenide perovskites have drawn significant attention as Pb-free alternatives. Chalcogenide perovskites are noteworthy due to the complete replacement of the halogen atom by a chalcogen, and the materials' proven environmental stability.[11] A handful of chalcogenide perovskites (generally based on the prototype $BaZrS_3$) have been synthesized, yet a successful PV device based on these materials has yet to be reported.[11–14] Our project has impacted this study, where $BaZrS_3$ has been extensively studied;[B] however, difficulties in depositing phase-pure thin-films without oxide inclusions has limited the development of thin-film solar cells.

Alternatively, the halogen atom does not need to be fully replaced and a mixed chalcohalide can (in principal) be synthesized. One especially interesting report, seeking to balance the favorable attributes of the silver bismuth iodides with those of silver bismuth sulfides, investigated possible mixtures to form silver bismuth chalcohalides.[15] Using FTO/c-TiO_2/mp-TiO_2/$Ag_aBi_bI_{a+3b}$/PTAA/Au devices wherein iodine was partially replaced by sulfur (best performance at 4 mol% sulfur) using a base composition of $Ag_3BiI_{6-2x}S_x$, they were able to achieve a significant boost in J_{sc} with a best PCE of ~5.6% for the

devices, despite a small cost in V_{oc}. Control *mesoporous* silver bismuth iodide cells also reached an average efficiency of ~4.3%, on par with the best solar cells previously reported using that material. These devices also displayed reasonably good shelf life in moderate (~40%) relative humidity, and refining surface properties, composition and device interfaces will likely yield further efficiency advances. Outside of $Ag_3BiI_{6-2x}S_x$, other reports of successful chalcohalides, particularly the Sb-based material $MASbSI_2$ have been shown to not be a phase-pure material, but rather $MA_3Sb_2I_9$ and Sb_2S_3.[X,16]

Interestingly, a family of perovskite-related materials, the "rudorffites," consisting of a network of edge-sharing metal-halide octahedra, show some promise for PV—particularly the silver bismuth iodides $Ag_aBi_bI_{a+3b}$. These compounds are reported to have a relatively low direct band gap of ~1.8 eV that is relatively insensitive to the Ag/Bi stoichiometry. Solar cells using a conventional mesoporous architecture deposited by solution processing have reached power conversion efficiency over 4%,[17] and in the current project, vacuum deposition led to nearly 1% PCE,[Z] making silver bismuth iodide the most promising non-Pb/Sn perovskite relative yet reported. This level of efficiency, in addition to relatively low band gap, make them a compelling candidate for further study.

Similar to the efforts in this project, no fully Pb-replaced perovskite or perovskite-related material has yet to attain the same high levels of performance enjoyed by the traditional hybrid lead-halide perovskites, demonstrating the extreme difficulty in achieving this goal.

Outside of moving towards Pb-free perovskite semiconductors, another avenue towards stable perovskite solar cells is to improve the contact layers within the perovskite device architecture. One key area of investigation relevant to the current project is that of inorganic hole transporting layers (HTLs). In an "inverted" device architecture (with an HTL as the front contact instead of an electron transporting layer, ETL), NiO_x has proven to be one of the highest-performing inorganic materials with reported device PCEs well above 18%.[18] Other inorganic materials in reasonably wide use as HTLs in high-performance perovskite solar cells include Cu_xO (reported PCE >16%[19]) and CuI (reported PCE >16%[20]). Other promising materials include transition metal oxides such as VO_x,[21] CoO_x,[22] WO_x,[23] and MoO_x,[23] all of which have been incorporated into moderately high-efficiency devices with PCEs ~13-15%. A perovskite solar cell using the delafossite oxide $CuGaO_2$ as HTL with efficiency >18% was reported in Dec 2016.[24] The reported work with $CuGaO_2$ inspired much of the work in the current project, where the researchers have fabricated perovskite solar cells using the novel delafossite $CuCrO_2$ as HTL with PCE reaching 14%.[V] Continued investigations of inorganic contact layers is a key aspect in the ultimate development of environmentally stable perovskite solar cells.

The work conducted within the project is on the leading edge of investigations into Pb-free perovskite materials as well as the push for developing stable Pb-based and Pb-free perovskite solar cells.

Introduction: In the current project the researchers have thoroughly studied a wide variety of Pb-based/Pb-free perovskites with wide ranging and impactful results (30 publications with citation numbers per article of up to 700 and >50 contributed, invited or keynote/plenary presentations). Specifically, the theoretical/experimental studies have screened a large swath of the possible halide, chalcohalide, and chalcogenide Pb-free perovskites for potential for solar cell applications, finding very few materials with high

solar cell potential within the reported space.[A-C,G,I,J,L-P,R,S,W-Z] Through first-principles investigations, this project has significantly advanced the understanding of the electronic structure and optical properties of perovskite materials, creating strong screening parameters for future experimental development.[K,M,P]

PV device studies were generally focused on Pb-containing perovskites due to the lack of promising Pb-free analogs. The researchers have demonstrated the impact of a thiocyanate treatment on perovskite solar cells,[F] the instability of CdS as a contact material,[H] and shown the promise of a novel HTL material, $CuCrO_2$.[V] On the other hand, two Pb-free, non-perovskite materials (InI and silver bismuth iodide) were shown to be successfully incorporated into solar cells by thermally evaporating the absorber material.[Y,Z] Each of these innovations will continue to have an impact on perovskite PV device research based on both Pb-based and Pb-free absorbers.

Project milestones and go/no-go points can be broken down into three groups: (1) Enhancement of Pb-based device performance and inorganic transport layers; (2) theoretical exploration of new perovskites and calculation of band offsets; and (3) experimental study of new perovskite semiconductors, thin-film deposition, and device incorporation/analysis. The breakdown of these groups into tasks and milestones is summarized in the table below where successful (unsuccessful) milestones and go/no-go points are labeled in green (red). Generally, this project has been very successful in its theoretical/experimental exploration of perovskite semiconductors with 30 publications resulting from the funding. However, as has been shown and will be outlined in the Results section, the goal of a high-performance Pb-free perovskite solar cell is still out of reach of this project and the wider perovskite community.

Group	Tasks	Milestones	Go/No-Go
Enhancement of Pb-based devices and inorganic transport layers	1, 5, 11	**1.1**: Pb-based perovskite solar cells will be demonstrated with efficiency above 8% **1.2**: Perovskite solar cells will be demonstrated with enhanced fill factor (target > 0.72) and efficiency at or above 12% **1.3**: State-of-the-art perovskite solar cells will be demonstrated with improved fill factor (target > 0.78) and efficiency at or above 15%	**1.4**: A Pb-based perovskite solar cell will be demonstrated with enhanced fill factor (target > 0.72), VOC over 0.85 V, and efficiency at or above 12%
		5.1: State-of-the-art perovskite solar cells will be demonstrated with improved fill factor (>0.80) and efficiency at or above 18%	
		11.1: Perovskite solar cells with inorganic HTL will be targeted with fill factor maintained at or above the level for the organic analog with efficiency at 16% or higher **11.2**: Submission of manuscript on the perovskite devices with inorganic HTLs.	
Theoretical exploration of new perovskites and calculation of band offsets	2, 3, 6, 7, 9, 13, 15	**2.1**: No less than 6 compounds will be investigated. Down select at least 3 target compounds for further theoretical analysis of electronic and optical properties	
		3.1: Optoelectronic properties will be calculated for ≥3 promising compounds	
		6.1: Down select at least 4 additional target compounds for further theoretical analysis	

		7.1: Paper will be submitted detailing at least 2 down-selected materials for further study	
		9.1: Elucidate defect properties for top 4 candidate compounds	
		13.1: Submit manuscript in refereed journal on band offset calculations	
		15.1: Submit ≥2 manuscripts on new perovskite materials, integrating computational and experimental results	
Experimental study of new perovskite semiconductors, thin-film deposition, and device incorporation/analysis	4, 8, 10, 12, 14, 15, 16, 17	**4.1**: At least one promising candidate will be identified for incorporation as an alternative absorber material in PV devices	**4.2**: At least one promising candidate will be identified for incorporation as an alternative absorber material in PV devices.
		8.1: Demonstrate film deposition of Pb-based and alternative perovskite films	
		10.1: Non-Pb/Sn perovskite-related solar cell with efficiency ≥5% or reduced Pb (>20% substituted) perovskite solar cell with improved stability and efficiency ≥12%	**10.2**: Non-Pb/Sn perovskite-related solar cell with efficiency ≥5% or reduced Pb (>20% substituted) perovskite solar cell with improved stability and efficiency ≥12% **10.3**: Manuscript submitted for publication on modeling and/or experimental results of the project through the end of year 2
		12.1: Submit manuscript related to the successful demonstration and characterization of a non-Pb perovskite absorber. **12.2**: Non-Pb/Sn perovskite-related solar cell with efficiency ≥10% or reduced Pb (>20% substituted) perovskite solar cell with improved stability and efficiency ≥15%	**12.3**: Non-Pb/Sn perovskite-related solar cell with efficiency at or above 10% or reduced Pb (>20% substituted) perovskite solar cell with improved operational stability and efficiency at or above 15%
		14.1: Completion of system for examining stability of small area (at least 0.05 cm^2) perovskite-related devices under various atmospheres and temperatures **14.2**: Demonstrate stable perovskite system with un-encapsulated air stability tested on >20 small area (at least 0.05 cm^2) devices and demonstrating <20% degradation after 1000 hr **14.3**: Down select at least one candidate for final optimization in year 4 of the project based on highest stability and efficiency criteria	**14.4**: Down select at least one candidate for final optimization thrust in year 4 of the project based on highest stability and efficiency criteria **14.5**: Demonstrate a perovskite system with un-encapsulated air stability tested on >10 small area (at least 0.05 cm^2) devices and yielding on average <20% degradation after 500 hr operation
		15.1: Submit ≥2 manuscripts on new perovskite materials, integrating computational and experimental results	
		16.1: Development of thin-film deposition capabilities and full characterization for ≥1 of the compounds explored in Task 15 followed by down-selection for PV device integration. **16.2**: Non-Pb/Sn perovskite-related solar cell with efficiency at or above 10% or reduced Pb (>20% substituted) perovskite solar cell with improved stability and efficiency at 15%.	
		17.1: Non- or reduced-as Pb (>20% substituted) perovskite-related solar cell	

		demonstrating <20% degradation after 500 hr operation and efficiency >16%	

Project Results and Discussion:

Tasks 1 & 5. Pb-based perovskite cell demonstration and optimization

As a first project target, we aimed to demonstrate competitive (in 2014 timeframe) Pb-based perovskite solar cells in terms of overall performance and hysteresis. Devices of this type were based on a traditional mesoporous structure as shown in Figure 1(a). It consists of a glass substrate coated with a transparent conducting oxide (fluorine-doped tin oxide or FTO), an electron transporting layer (ETL, compact TiO_2) coupled with a mesoporous scaffold (TiO_2 nanoparticles), the hybrid perovskite absorber ($CH_3NH_3PbI_3$, $MAPbI_3$), a hole transport layer (HTL, Spiro-OMeTAD) and finally a top contact (Au).

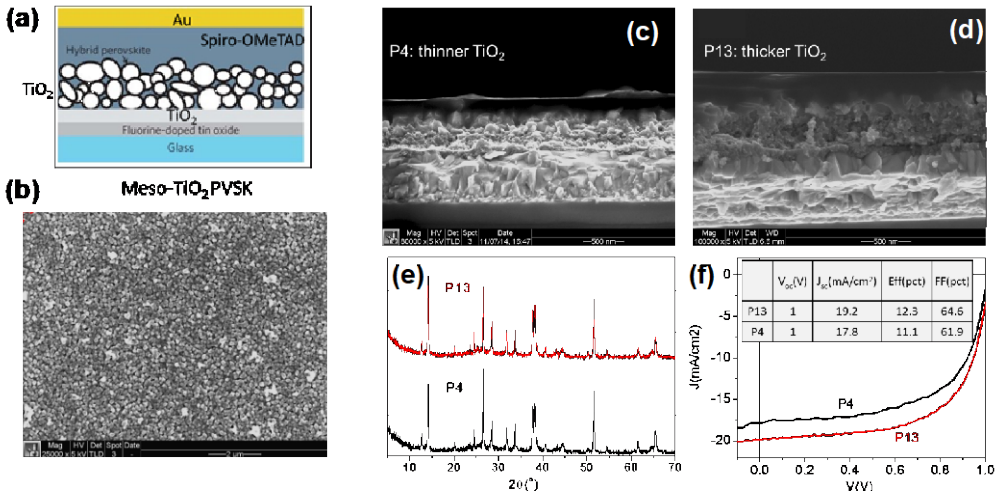

Figure 1. *(a) Schematic of the standard Pb-based device structure. (b) Top-view of the perovskite layer deposited on top of TiO_2. (c, d) Cross-sectional SEM images, (e) XRD scans and (f) J-V plots of top-performance cells with different mesoporous TiO_2 thicknesses, respectively. Inset in (f): the device parameters determined from the J-V characteristics. Note that the J-V measurement was conducted in the sweep direction that yields the lowest performance values (i.e., by hysteresis effects we can achieve higher efficiency if scanned in the opposite direction).*

The device fabrication method was generally based on published work with minor adjustments. Under ambient conditions, the compact TiO_2 precursor was spin-coated onto FTO substrates and the layer was dried at 150 ˚C for 10 minutes. The mesoporous (mp) TiO_2 layer was spin-coated from a suspension of TiO_2 nanoparticles in ethanol, which was then dried and sintered at 520 ˚C for an hour. Inside a N_2-filled glovebox, the perovskite ($MAPbI_3$) layer was deposited in a two-step process. First, a PbI_2 solution was spin-coated onto the mp-TiO_2 and dried. Then, a CH_3NH_3I (MAI) solution was dropped and spun onto the PbI_2-coated substrate and dried/reacted at 100 ˚C. The spiro-OMeTAD HTL was deposited by spin-coating the precursor and drying in ambient conditions overnight. To complete the device, the Au contact was deposited by thermal evaporation.

Initially, devices fabricated from this method exhibited small-grained $MAPbI_3$, with some inclusion of PbI_2 and MAI phases (light-colored grains) within the absorber layer as shown in Figure 1(b). As seen in Figures 1(c-f) the morphology of the perovskite layer and the

device performance of these devices was largely dependent on the thickness of the mp-TiO_2 layer, although this did not greatly affect the crystallinity of the perovskite as is evident in the X-ray diffraction (XRD) patterns. With this device structure and fabrication method, we achieved devices exhibiting 12.3% power conversion efficiency (PCE).

Further, we employed a planar structure (no mesoporous layer) to construct a full device. In addition to the replacement of the transporting layer (SnO_2/PCBM were used as electron transporting layers instead of TiO_2), a lead thiocyanate additive was found to significantly improve the grain structure (Fig. 2). The film grain size with thiocyanate additive is of order a few micrometers (Fig. 2(b), (d)), as opposed to a few hundred nanometers for the control without thiocyanate additive (Fig. 2(a), (c)). The resulting PbI_2 excess at grain boundaries helps reduce the dark current and shunting along these grain boundaries in the devices.

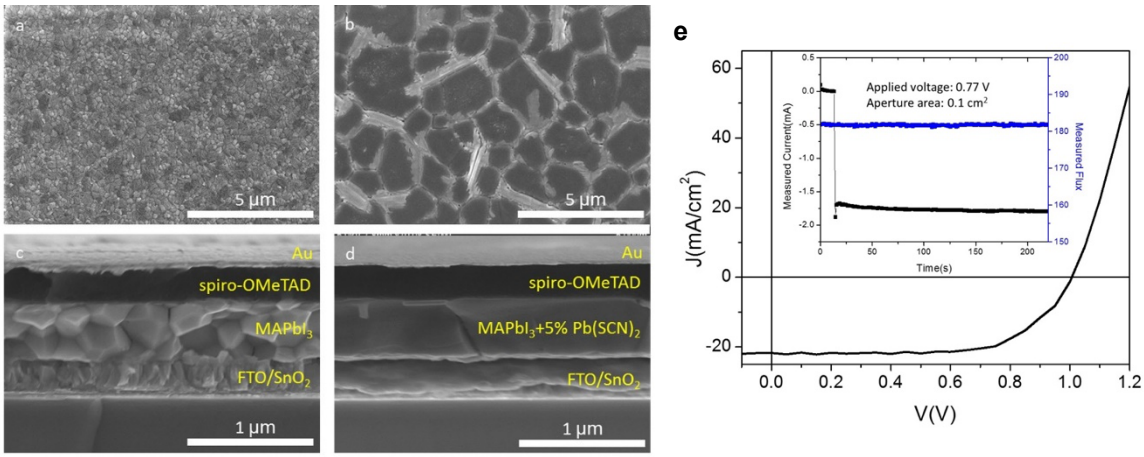

Figure 2. *Top-view SEM of $MAPbI_3$ films (a) without and (b) with 5% $Pb(SCN)_2$ in the precursor; Cross-sectional SEM of completed devices using $MAPbI_3$ (c) without and (d) with 5% $Pb(SCN)_2$ in the precursor. (e) Current density-voltage (J-V) characteristic of one of our cells (V_{oc}: 1V, J_{sc}: 21.8 mA/cm^2, FF: 0.68, PCE: 14.8%). The inset shows the steady-state photocurrent at maximum power point (0.77V), and the resulting stabilized power conversion efficiency is 13.8%.*[F]

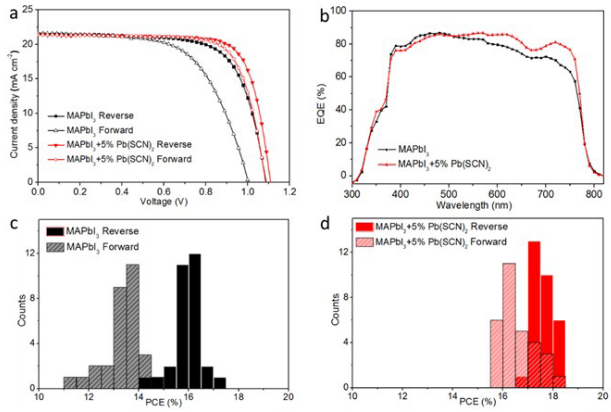

Figure 3. *(a) J–V curves of the perovskite solar cells using $MAPbI_3$ with and without 5% $Pb(SCN)_2$ in the perovskite precursor, under reverse and forward voltage scanning. (b) Corresponding EQE spectra. Histogram data of PCEs for 30 solar cells using $MAPbI_3$ (c) without and (d) with 5% $Pb(SCN)_2$.*[F]

Figure 3(a) shows the *J–V* curves of two representative cells using perovskite absorbers with and without 5% $Pb(SCN)_2$ in the precursor under reverse and forward voltage scanning. In addition, the EQE spectra and the histogram data of the PCEs of 30 solar

cells made with both conditions are displayed in Fig. 3(b-d). It can be seen that thiocyanate addition improves the fill factor significantly and the non-radiative recombination is greatly reduced, as indicated by the increased near-infrared response in the quantum efficiency. As a result, we were able to obtain devices with stabilized efficiency >18% and this work was published in *Advanced Materials*.[F]

Task 2 & 6: Determine structural stability of new perovskite absorbers & electronic and optical properties of new perovskite absorbers.

In this task, we have explored the energetic stability of various new chalcohalide and halide perovskite-type compounds through density functional theory (DFT) calculations.

Pb-free chalcohalide perovskites: We have considered alternative perovskite compounds containing Bi (instead of Pb), a metal with lone-pair s states. To maintain charge neutrality (given that Bi is trivalent vs divalent), the new perovskites have the formula $ABX^{I}X^{II}_2$ or $ABX^{I}_2X^{II}$, where A is a Cs or Ba cation and X^{I} and X^{II} are chalcogen and halogen anions. The DFT calculations were performed using the VASP code, the standard frozen-core projector augmented-wave (PAW) method, and a cut-off energy for the basis functions of 400 eV. The general gradient approximation (GGA) was used for exchange-correlation. Atomic positions were relaxed until the forces on the atoms were below 0.05 eV/Å. While the effect of spin-orbit (SOC) was not considered due to the high demand on computing power, this should not significantly affect the conclusions on the material *stability*.

The atomic structure of a quaternary perovskite $ABX^{I}X^{II}_2$ is more complex than an ideal perovskite ABX_3. The two anion elements, X^{I} and X^{II}, can exhibit structural ordering and disordering, affecting the stability significantly. We have first studied the stability of ordering in $CsBiOF_2$. We have considered a variety of ordered structures between the halogen and chalcogen atoms.[C] It was found that the structures with the Bi-O *cis*-chains (*cis*-chain means that the angle between O-Bi-O is 90°) have much lower energies than the fully ordered perovskite. This observation strongly indicates that the highly ordered structures are not energetically stable. The situation is similar to that in the $SrTaO_2N$ perovskite, in which Sr-O *cis*-chains are energetically preferred.[25]

To evaluate the prospective new perovskite compound stability, we calculated the reaction energies (all calculated using the lowest energy *cis* chain configuration mentioned above), considering various possible pathways—e.g., $CsBiOCl_2$ may be synthesized by reaction of $CsCl+Bi_2O_3+BiCl_3$. If the reaction energy of $3CsCl+Bi_2O_3+BiCl_3 \rightarrow 3CsBiOCl_2$ is negative, then the formation of $CsBiOCl_2$ is not preferred. However, there are multiple possible formation pathways. If all possible reactions show positive reaction energies, the compound is considered stable without likely impurity formation. If one of the reactions shows a negative energy, the compound is considered not stable. All considered $ABX^{I}X^{II}_2$ or $ABX^{I}_2X^{II}$ perovskites show negative decomposition energies (Table 1), indicating that these perovskites may not be synthesized experimentally under equilibrium conditions. This work was published in the *Journal of Physical Chemistry C*.[C]

Table 1. *Calculated reaction energy change of quaternary perovskites (Unit: eV per formula unit). If one reaction shows negative energy, no other pathways are explored.*[C]

X:	F_2	Cl_2	Br_2	I_2	X:	F	Cl	Br	I
$CsBiOX_2$	-0.09	-0.36	-0.12	-0.31	$BaBiO_2X$	-0.02	-0.01	-0.03	-0.02
$CsBiSX_2$	-0.37	-0.03	-0.19	-0.29	$BaBiS_2X$	-0.44	-0.57	-0.32	-0.24
$CsBiSeX_2$	-0.51	-0.14	-0.27	-0.34	$BaBiSe_2X$	-0.61	-0.68	-0.47	-0.37
$CsBiTeX_2$	-0.32	-0.41	-0.51	-0.53	$BaBiTe_2X$	-0.98	-1.00	-0.90	-0.68
$CsSbOX_2$	-0.02	-0.12	-0.07	-0.28	$BaSbO_2X$	-0.03	-0.09	-0.04	-0.06
$CsSbSX_2$	-0.10	-0.12	-0.14	-0.25	$BaSbS_2X$	-0.37	-0.39	-0.26	-0.19
$CsSbSeX_2$	-0.60	-0.24	-0.22	-0.31	$BaSbSe_2X$	-0.55	-0.63	-0.45	-0.33
$CsSbTeX_2$	-0.65	-0.52	-0.47	-0.51	$BaSbTe_2X$	-0.89	-0.96	-0.85	-0.66

Pb-free chalcogenide perovskites: In addition to mixed chalcohalides and Pb-free halide perovskites, we studied the theoretical stability of chalcogenide perovskites. Recently, chalcogenide perovskites ABX_3 (X = S, Se; A, B = metals with combined valence of 6), which are more environmentally-friendly as compared to lead halide perovskites, have been proposed for PV applications, some of which have been synthesized. However, only $CaZrS_3$, $CaHfS_3$, $BaZrS_3$, and $BaHfS_3$ are found to exist in the distorted 3D perovskite phase. The calculated bandgaps for these perovskites are about 1.96, 2.30, 1,76, and 2.02 eV, respectively. Among these sulfide perovskites, only $BaZrS_3$ exhibits a bandgap that is close to the range suitable for making efficient single-junction solar cells.

The bandgap of $BaZrS_3$ is slightly larger than optimal for single junction solar cells. However, the bandgap should be tunable through alloying with isovalent elements Ti and/or Se. We have therefore studied the stability of $BaZr_{1-x}Ti_xS_3$ alloys by calculating the energies needed to decompose the alloys back to the binary phases or the unalloyed ternary phases using the GGA functional. Based on literature reports, perovskite and hexagonal structures are considered for $BaZrS_3$ and $BaTiS_3$, respectively. As shown in Table 2, the $BaZr_{1-x}Ti_xS_3$ alloys do not decompose into binary phases. However, for Ti concentrations >25%, the calculated decomposition energies are negative, meaning that they should decompose into the unalloyed ternary phases. Therefore, our calculated results suggest that it will be difficult to synthesize $BaZr_{1-x}Ti_xS_3$ alloys under thermal equilibrium growth conditions (consistent with our experimental efforts). This work has appeared in *Chemistry of Materials*.[B]

Table 2. *Calculated decomposition energies for $BaZr_{1-x}Ti_xS_3$ alloys relative to prospective binary and ternary phases. Positive values indicate a stable alloyed phase.*[B]

$BaZr_{1-x}Ti_xS_3$	Binary phases (eV)	Ternary phases (eV)
$BaZrS_3$	0.221	-
$BaZr_{0.75}Ti_{0.25}S_3$	0.242	0.013
$BaZr_{0.5}Ti_{0.5}S_3$	0.168	-0.067
$BaZr_{0.25}Ti_{0.75}S_3$	0.118	-0.124
$BaTiS_3$	0.249	-

Pb-free halide double perovskites: Further, we have studied the stability for several other prospective perovskite absorbers, including the halide double perovskites $Cs_2AgBiBr_6$ and Cs_2AgBiI_6 using DFT calculations. The calculations were performed using the VASP code with the standard frozen-core projector augmented-wave (PAW) method. The cut-off energy was 400 eV. GGA was used for exchange-correlation. Atomic positions are relaxed, with all the forces on the atoms below 0.01 eV/Å.

To stabilize $Cs_2AgBiBr_6$, the chemical potentials ($\Delta\mu$) should reach the following thermodynamic equilibrium:

$$2\Delta\mu_{Cs} + \Delta\mu_{Ag} + \Delta\mu_{Bi} + 6\Delta\mu_{Br} = \Delta H(Cs_2AgBiBr_6) = -11.36 \text{ eV}, \quad (1)$$

where $\Delta H(Cs_2AgBiBr_6)$ is the formation enthalpy of $Cs_2AgBiBr_6$ as referred to the elemental Cs, Ag, Bi and Br_2 phases. Furthermore, the formation of secondary phases including CsBr, $CsBr_3$, AgBr, $BiBr_3$, $CsAgBr_2$, Cs_2AgBr_3, and $Cs_3Bi_2Br_9$ must be avoided.

Under these constraints, the stable region of $Cs_2AgBiBr_6$ is bound in a polyhedron (Figure 4(c)). The polyhedron exhibits a long but narrow shape, indicating the chemical synthesis must be carefully controlled to obtain single-phase $Cs_2AgBiBr_6$, similar to other halide perovskites. The stability of $Cs_2AgBiBr_6$ can also be evaluated by the calculated decomposition energy. We tested many possible decomposition pathways into secondary phases, and found that the decomposition into $CsAgBr_2$, AgBr, and $Cs_3Bi_2Br_9$ shows the lowest decomposition energy (E_d) of 0.11 eV per formula unit, which is consistent with the narrow shape of the polyhedron in Figure 4(c).For hypothetical Cs_2AgBiI_6, the lowest E_d was estimated to be –0.47 eV per formula unit for decomposition to $CsAg_2I_3$ and $Cs_3Bi_2I_9$, indicating that Cs_2AgBiI_6 is difficult to synthesize under thermodynamic equilibrium conditions, which may explain why there have been no experimental reports of successful synthesis of pure Cs_2AgBiI_6 and the literature has focused on the Br analog instead.

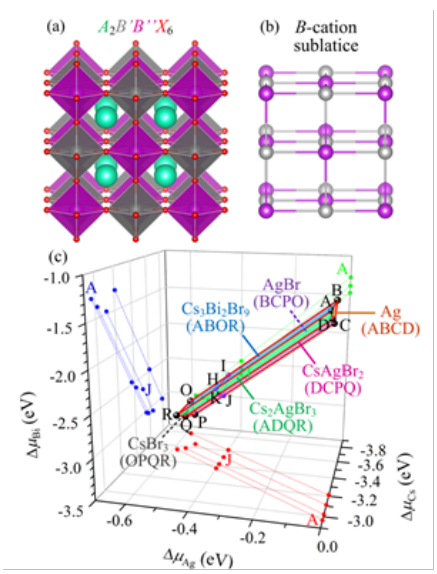

Figure 4. *(a) Crystal structure and (b) B-cation sublattice of double perovskites $A_2B'B''X_6$ (space group Fm–3m). (c) Calculated polyhedron of the chemical potential region where $Cs_2AgBiBr_6$ is stable against possible competitive phases, including Cs, Ag, Bi, Br_2, CsBr, $CsBr_3$, $BiBr_3$, $CsAgBr_2$, Cs_2AgBr_3, and $Cs_3Bi_2Br_9$.*[l]

Task 3 & 7: Electronic and optical properties of new perovskite absorbers

In Tasks 3 and 7, we calculated the electronic and optical properties of various promising perovskite materials, taking into account the results of the DFT stability calculations performed in the previous Tasks.

Pb-free chalcohalides and halide perovskites: Based on the above thermodynamic stability results from Tasks 2/6, we calculated the electronic/optical properties of $CsBiOF_2$ and $Cs_3Sb_2I_9$. Figure 5(a) shows the calculated bandgaps and formation enthalpies of $CsBiOF_2$ with various orderings. Due to the large unit cells, hybrid functional (HSE) and SOC are not considered, meaning some errors in absolute values are expected (however, trends should be reliable). It is seen that both bandgaps and formation enthalpies depend on the O-F ordering. Such ordering-induced bandgap variation may be detrimental to PV performance, as they may introduce bandgap variations and lead to large Urbach tails.

The band structures of three ordered structures, Apical-I, Apical O-II, Apical O-III, appear in Figure 5(b). The structures exhibit bandgaps suitable for solar cell applications and the band structures exhibit similar features. Both the valence/conduction bands strongly disperse, which is favorable for charge transport. These band structures reinforce the potential of $CsBiOF_2$ for PV applications.

(a)

Structure	Bi-O *Cis*-chain	Eg (eV)	ΔE (meV/f.u.)
Pseudo-cubic I	No	0.14	0
Pseudo-cubic II	Yes	0.94	-434
Pseudo-cubic III	Yes	1.08	-440
O-equatorial	No	0.07	33
O-apical	No	0.16	2
Apical O-I	Yes	1.4	-435
Apical O-II	Yes	1.08	-438
Apical O-III	Yes	1.1	-449
Apical O-IV	Yes	1.4	-440
Equatorial O-I	Mixed	0.46	-188
Equatorial O-II	Yes	1.08	-432
Equatorial O-III	Yes	1.14	-452
Equatorial O-IV	No	0.3	85
3D *cis*-chain-I	Yes	1.29	-487
3D *cis*-chain-II	Yes	1.65	-484
Full disorder	No	1.21	-300

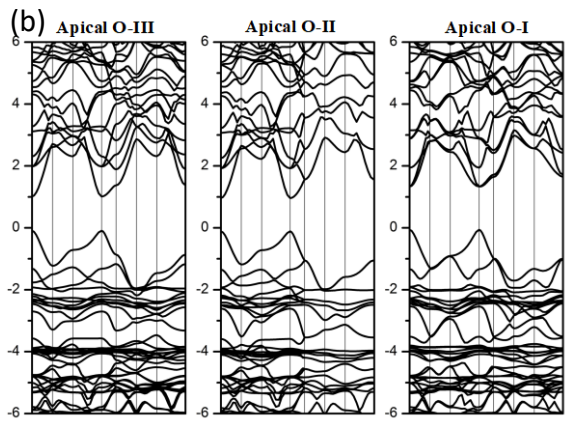

Figure. 5. *(a) Calculated formation enthalpy and bandgap of $CsBiOF_2$ with various ordered structures. (b) Calculated band structures of three ordered structures of $CsBiOF_2$: Apical-I, Apical O-II, Apical O-III (see Figure 6 for details of structure).*[C]

In order to gain better insight into the electronic, optical and defect properties of the second material, $Cs_3Sb_2I_9$, we performed DFT band structure calculations for the two known structures, dimer and layered (Fig. 6(a)). The layered structure has an HSE-calculated nearly direct gap of 2.06 eV, in good agreement with the experimental 2.05 eV value (see below), while a larger indirect 2.40 eV gap was found for the dimer structure.

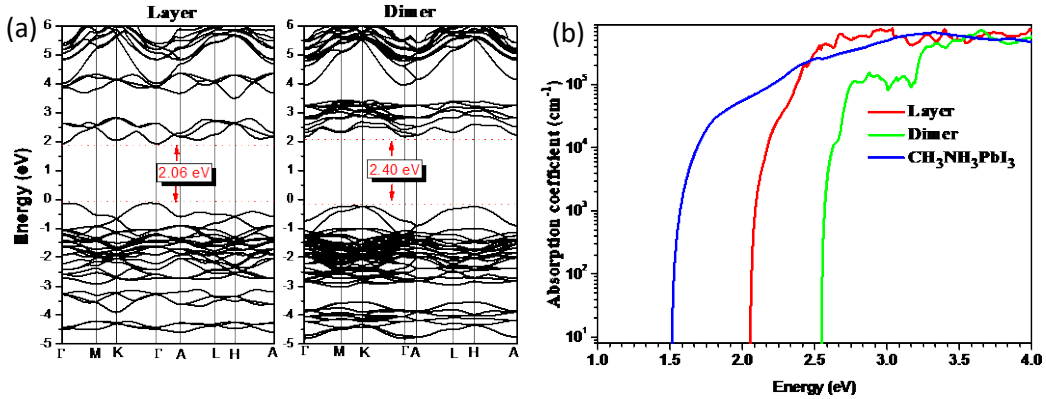

Figure 6. *HSE calculated band structures of $Cs_3Sb_2I_9$ in layered and dimer modifications (a) and*

calculated absorption coefficients for $Cs_3Sb_2I_9$ with the layered and dimer structures as compared to that of $CH_3NH_3PbI_3$ (b).[A]

The optical absorption coefficients for $Cs_3Sb_2I_9$ in both structures have been calculated in comparison to $CH_3NH_3PbI_3$ (Fig. 6(b)). The absorption coefficients of both layered and dimer structures are as high as that of $CH_3NH_3PbI_3$; however, the onset energy of each phase is larger than that for $CH_3NH_3PbI_3$. Such high absorption coefficients for the $Cs_3Sb_2I_9$ phases can be understood, since the valence bands are comprised of I *p* + Sb *s* orbitals and the conduction bands are derived from Sb *p* orbitals. Thus, the optical transitions are expected to be from (I *p* + Sb *s*) to Sb *p*. This suggests there is potential for PV applications for $Cs_3Sb_2I_9$, especially in the layered structure.

Pb-free chalcogenide perovskites based on $BaZrS_3$: Further, we calculated the electronic and optical properties of the chalcogenide perovskite $BaZrS_3$ and its alloyed variations, $BaZr_{1-x}Ti_xS_3$ and $BaZrS_{3-x}Se_x$. The GGA+*U* calculated band structure and $BaZrS_3$ density of states are shown in Fig. 7. It is seen that $BaZrS_3$ exhibits a direct band gap at the Γ(0,0,0) point. The valence band is mainly derived from S 3*p* states with a small component of Zr 4*d* in the valence band, suggesting there is a weak antibonding between Zr 4*d* and S 3*p*, leading to antibonding states at the valence band maximum (VBM). Both conduction and valence band edges exhibit dispersive bands, suggesting small carrier effective masses. Our GGA+*U* calculated results agree well with those calculated by HSE, suggesting that GGA+*U* is reliable to calculate the electronic, optical, and defect properties of chalcogenide perovskites.

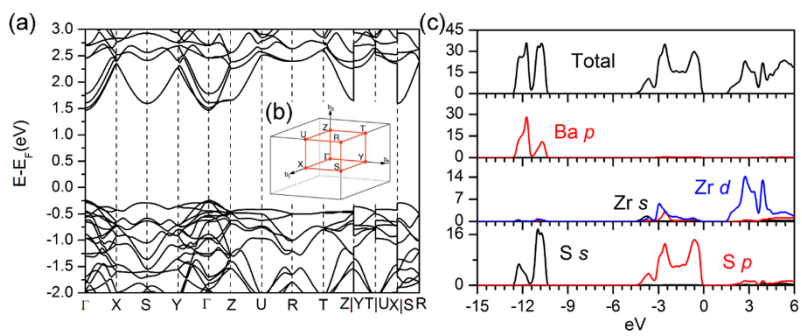

Figure 7. *GGA+U calculated band structure and density of states (DOS) for $BaZrS_3$.*[B]

Because the conduction and valence bands are derived mainly from the Zr 4*d* and S 3*p* states, respectively, the bandgap of $BaZrS_3$ can be lowered by alloying with isovalent elements that exhibit either *d* states lower in energy than Zr 4*d* states or *p* states higher in energy than the S 3*p* states. Considering atomic size and electronegativity mismatch, Ti and Se are the first choices for alloying of $BaZrS_3$. The calculated GGA+*U* bandgaps of $BaZr_{1-x}Ti_xS_3$ and $BaZrS_{3-x}Se_x$ alloys are shown in Fig. 8.

It is seen that alloying with both Ti and Se can lower the bandgap of $BaZrS_3$. While the bandgap decreases nearly linearly with Ti content, the trend in Se alloying has a bowing effect and does not reduce the bandgap as effectively. With ~10% Zr substitution, the bandgap is already reduced to <1.50 eV. To achieve a similar bandgap, 30% S has to be substituted by Se. Experimental results have shown that $BaZr_{0.75}Ti_{0.25}S_3$ exists in the perovskite structure only at high temperatures (900°C) and under pressures (60 kBar), with large substitutions not being stable, suggesting that ambient pressure synthesis of the alloyed perovskite should be limited to low Ti substitutions.

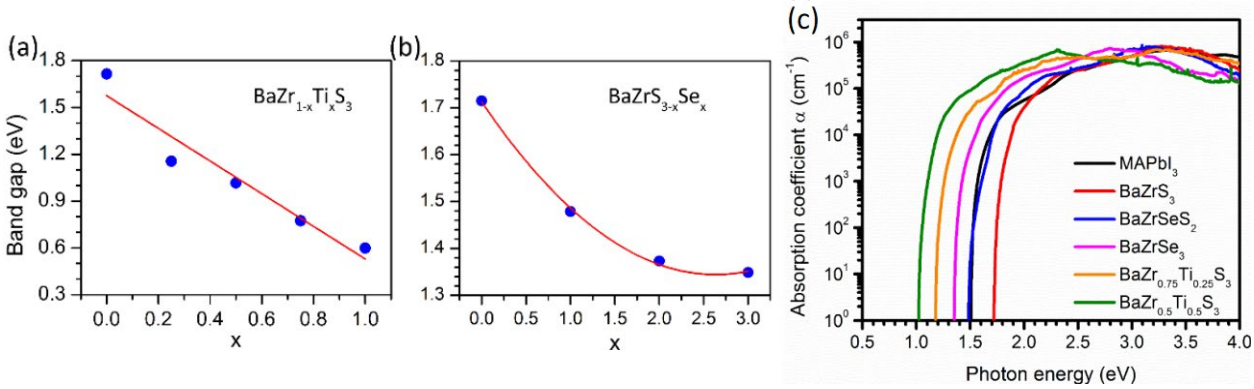

Figure 8. *Calculated GGA+U bandgaps of (a) $BaZr_{1-x}Ti_xS_3$ and (b) $BaZrS_{3-x}Se_x$ alloys. (c) Calculated optical absorption coefficients of $CH_3NH_3PbI_3$ and $BaZrS_3$–based perovskite alloys.*[B]

To view the benefits of Ti and Se alloying, we have calculated the optical absorption coefficients of $BaZr_{1-x}Ti_xS_3$ and $BaZrS_{3-x}Se_x$ alloys with representative compositions. As shown in Fig. 8(c), alloying with Ti and Se only reduces the bandgap and does not impact the absorption coefficient magnitude. The optical absorption of chalcogenide perovskites arises from the *p-d* transitions, which have a higher joint density of states compared with the *p-p* transitions seen in other perovskites. Therefore, the optical absorption coefficients of chalcogenide perovskite alloys are even higher. As a result, chalcogenide perovskite devices should be able to use very thin absorbers to achieve high efficiencies.

Two-dimensional perovskite $(CH_3NH_3)_2Pb(SCN)_2I_2$: We performed DFT calculations to study the electronic structure and optical properties of the 2D $MA_2Pb(SCN)_2I_2$ perovskite using the Perdew–Burke–Ernzerhof (PBE) functional and the HSE+SOC approach. The PBE non-SOC (HSE+SOC) method predicts a direct bandgap of 2.11(2.12) eV and an indirect bandgap of 2.05(2.06) eV. Both PBE non-SOC and HSE+SOC predict that the difference between the direct/indirect bandgap is as small as 0.06 eV. These calculated bandgaps agree well with experimental values—2.11 eV (direct) and 2.04 eV (indirect).

Though both the PBE and HSE+SOC calculations may correctly predict the perovskite band gaps, the latter better interprets the conduction band of these perovskites as it accounts for the SOC-induced splitting of the Pb 6*p* states. Therefore, we discuss the band structure of 2D $MA_2Pb(SCN)_2I_2$ based on the HSE+SOC method. Figs. 9(a, b) show the crystal structure of the orthorhombic 2D $MA_2Pb(SCN)_2I_2$ and the corresponding first Brillouin zone. Fig. 9(c) shows the calculated band structure along the *k*-path shown by the red line in Fig. 9(b). Fig. 9(d) shows the calculated total and site-projected density of states. The VBM consists mainly of I 5*p*/S 3*p*–Pb 6*s* antibonding states, while Pb 6*p* states dominate the CBM. The lower conduction band exhibits clear SOC-induced splitting.

The calculated band structure for *$MA_2Pb(SCN)_2I_2$* (Fig. 9(c)) reveals dispersive character for the lower conduction band and upper valence band parallel to the octahedral layers. This dispersive feature can be understood by the strong I 5*p* S 3*p*–Pb 6*s* antibonding coupling, similar to 3D $MAPbI_3$. The calculated effective masses for holes and electrons along the T–Z (i.e., [010]) direction are 0.99 m_0 and 0.88 m_0, respectively, and those along the T–Y (i.e., [001]) direction are 2.36 m_0 and 0.34 m_0, respectively. However, there is almost no dispersion for the states near the CBM and VBM along the T–R direction (i.e., [100]), which is attributed to the lack of octahedra connectivity along this direction.

Figure 9(e) shows the PBE calculated absorption coefficient for $MA_2Pb(SCN)_2I_2$, exhibiting a strongly anisotropic character due to the layered structure. The absorption contribution along the [100] direction crossing the layers (α_{xx}) is much weaker than that along the [010] and [001] directions parallel to the layers (α_{yy}, and α_{zz}, respectively). The absorptions along the [010] and [001] directions exhibit a peak at 2.18 eV, right above the absorption edge, consistent with the experimental optical spectra. Due to the *p–p* transitions, 2D $MA_2Pb(SCN)_2I_2$ exhibits a high absorption coefficient. Therefore, it may still be considered for use as the top cell of tandem solar cell applications. The above work on $MA_2Pb(SCN)_2I_2$ is published in the *Journal of Physical Chemistry Letters.*[E]

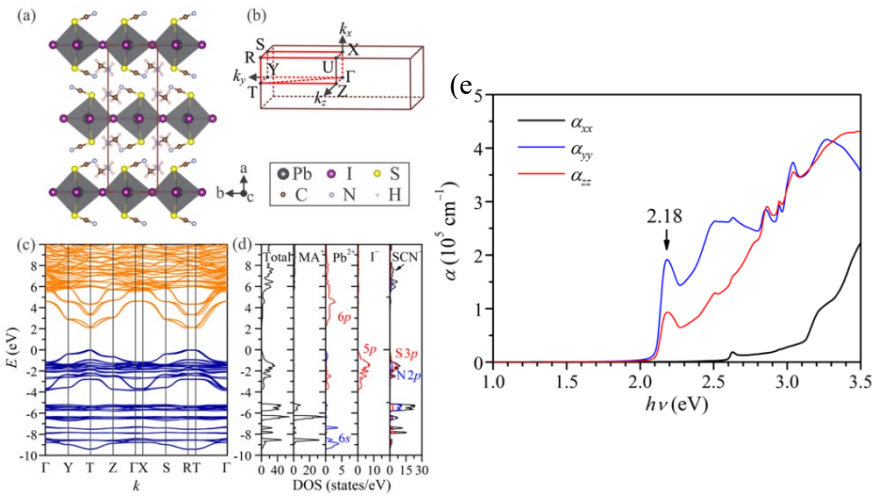

Figure 9. *(a) Crystal structure, (b) first Brillouin zone for the and the k-path (red line) used to plot the band structure, (c) band structure and (d) density of states calculated with HSE+SOC, and (e) calculated optical absorption of orthorhombic $MA_2Pb(SCN)_2I_2$.*[E]

<u>*Double perovskite $Cs_2AgBiBr_6$*</u>: Figures 10(a),(b) show the PBE non-SOC band structure and density of states of $Cs_2AgBiBr_6$, respectively. The PBE non-SOC method predicts an indirect bandgap of 1.32 eV, which is smaller than the experimental value of 1.95 eV. The VBM is located at the X point and the CBM is located at the L point. The VBM consists of antibonding states of Br 4*p* and Ag 4*d* orbitals. The Bi 6*s* lone-pair orbitals are located at 10.2 eV below the VBM and have no significant contribution to the VBM. The CBM is mainly composed of Bi 6*p* orbitals and slightly of Ag 5*s* and Br 4*p* orbitals. Previous reports have shown that, for lead halide perovskites, the HSE hybrid functional with inclusion of spin–orbit coupling effect (HSE+SOC) can correctly predict the bandgaps and interpret well the lower conduction bands derived from Pb 6*p* states. Therefore, the HSE+SOC method was used to examine the electronic structure of $Cs_2AgBiBr_6$ (Figs. 10(c),(d)). The HSE+SOC method predicts an indirect bandgap of 1.97 eV, reproducing the experimental observation. The lower conduction band exhibits a clear SOC-induced splitting of Bi 6*p* (Fig. 10(c)), which lowers the bandgap by 0.24 eV compared with that calculated by the HSE non-SOC method (2.21 eV). With the HSE+SOC band edges, the effective masses for holes are calculated to be 0.24 m_0 along the X–Γ direction and 0.96 m_0 along the X–W direction and those for electrons are 0.58 m_0 along the L–Γ direction and 0.34 m_0 along the L–W direction, suggesting good carrier transport properties.

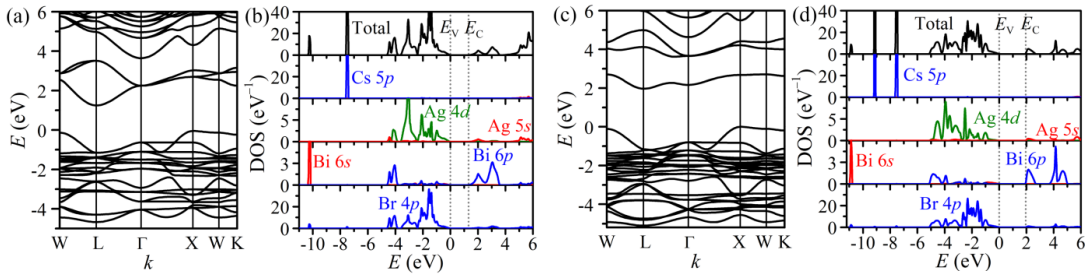

Figure 10. *Band structures and total and projected densities of states (DOSs) of $Cs_2AgBiBr_6$ calculated with the (a,b) PBE non-SOC and (c,d) HSE+SOC methods.*[1]

Task 4: Empirical study of new perovskites

In this Task, we have targeted the synthesis and deposition of multiple novel Pb-free or Pb-reduced perovskite semiconductors by experimental methods. The compounds targeted generally included two classes of compounds: mixed chalcogenide-halide compositions $ABChX_2$ and $A'BCh_2X$ (A = Cs^+, $CH_3NH_3^+$; A' = Ba^{2+}; B = Sb^{3+} or Bi^{3+}; Ch = O^{2-}, S^{2-}, Se^{2-}, Te^{2-}; X = F^-, Cl^-, Br^-, I^-), and mixed B-cation compositions $A_2BB'X_6$ (A = Cs^+; B = Sb^{3+} or Bi^{3+}; B' = Na^+, Cu^+, Ag^+; X = F^-, Cl^-, Br^-, I^-). Both groups of compounds involve replacement of the toxic heavy metal Pb in the lead halide perovskites and possibly offer greater environmental stability due to the covalent bonding of chalcogens.

In an attempt to prepare the desired compositions, we employed solid state and solution synthesis methods demonstrating the presence of several very stable phases in the target systems, most notably $A_3B_2X_9$ compounds. The most promising member among the $A_3B_2X_9$ compounds is $Cs_3Sb_2I_9$, whose layered form has a 2.05 eV band gap. We developed a two-step deposition approach to fabricate high quality layered $Cs_3Sb_2I_9$ thin films (Fig. 11(a,b)). By carefully controlling the (post-)deposition treatments, we prepared *c*-axis oriented and randomly oriented films (Fig. 11(d,e)). The obtained films show enhanced stability under moist air (relative humidity 20-50%) compared to $CH_3NH_3PbI_3$ films. Only a modest evolution of CsI impurity peak is noticeable for both $Cs_3Sb_2I_9$ film orientations after 60 days in ambient air.

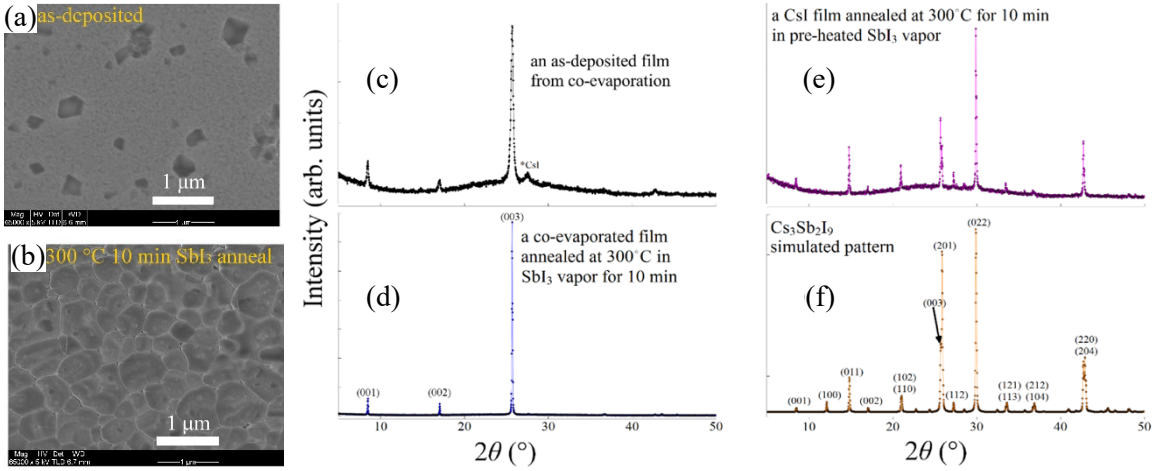

Figure 11. *Scanning electron microscopy images of (a) as-deposited and (b) annealed thin films of the layered $Cs_3Sb_2I_9$. (a) The initial film is deposited through co-evaporation of CsI and SbI_3, which is followed by annealing on a hot plate under a quartz cover inside a nitrogen-filled glove box at (b) 300 °C. (c-e) Powder X-ray diffraction patterns (Cu-Kα radiation) of layered $Cs_3Sb_2I_9$*

films, which were subjected to various thermal treatment procedures compared to the simulated diffraction pattern (f).[A]

However, despite promising band structure and optoelectronic properties, and enhanced stability, we found that the photoluminescence (PL) peak is suppressed for our $Cs_3Sb_2I_9$ films (Fig. 12). The origin of weak PL is attributed to deep defects for this compound based on our computational work and could also be related to a slightly indirect nature of the band gap (difference between the direct and indirect gaps is <20 meV). Therefore, in order to use layered $Cs_3Sb_2I_9$ as a PV material, careful control of defects is necessary.

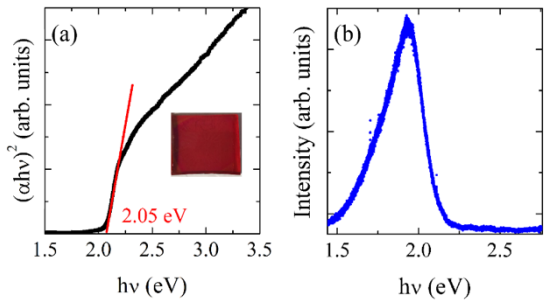

Figure 12. *(a) Band gap of the layered modification of $Cs_3Sb_2I_9$ (inset shows a thin film) was calculated to be 2.05 eV from absorbance data using the Tauc relation. (b) A photoluminescence spectrum of $Cs_3Sb_2I_9$ obtained using 442 nm laser excitation.*[A]

Besides $Cs_3Sb_2I_9$, we have targeted syntheses of various other hypothetical chalochalide and halide perovskite absorbers. Each of the targeted compounds had a Goldschmidt tolerance factor in a reasonable range, but very few compounds formed the desired phase. Indeed, the only phases that were stable under syntheses were those of the known perovskite 329 and 216 stoichiometries. Some of these that were stable have been pursued for further exploration through thin-film deposition studies as will be summarized in the next section. These results are published in the *Journal of Physical Chemistry C.*[C]

Task 8: Thin film deposition

During this Task, a variety of film deposition methods were developed for Pb-free halide and chalcogenide perovskites, including $Cs_3Sb_2I_9$, Cs_2SnI_6 and $BaZrS_3$.

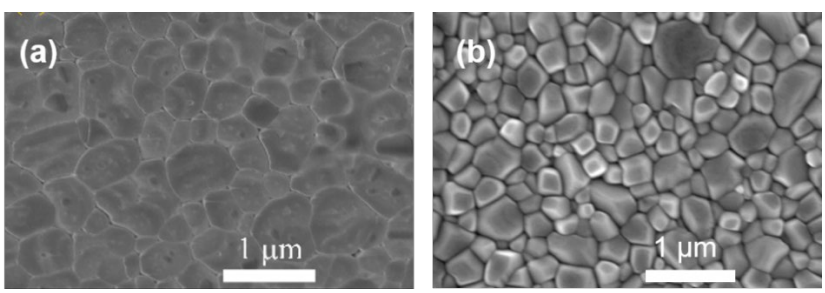

Figure 13. *Plane-views of (a) $Cs_3Sb_2I_9$ and (b) Cs_2SnI_6 films as lead-free perovskite materials prepared by a two-step method.*[A,G]

$Cs_3Sb_2I_9$ and Cs_2SnI_6 compounds have been proposed as Pb-free and relatively air-stable perovskite materials. As these compounds do not contain divalent Sn ions, self-doping widely observed in $CH_3NH_3SnI_3$ materials can be prevented. Thin-films of both compounds were prepared by a two-step method. First, to deposit $Cs_3Sb_2I_9$ films, CsI and SbI_3 were evaporated on substrates. The as-deposited films were annealed in SbI_3 vapor. By post-annealing at 300 °C for 10 min, small crystallites in the as-deposited film became larger without pin-hole defects as seen in Figure 13(a). Likewise, Cs_2SnI_6 films were grown by evaporating CsI layers followed by annealing in preheated SnI_4 vapor at 190

°C. As a result, high-quality Cs_2SnI_6 films were obtained as depicted in Fig. 13(b). The results of the film deposition studies have been published in *Chemistry of Materials.*[A, G]

As discussed above, $BaZrS_3$ is a potential candidate for a lead-free, air-stable and 3D perovskite material.[13] For $BaZrS_3$ film deposition, a precursor layer was prepared by co-sputtering BaS and Zr sources. The precursors were then annealed at 580~590 °C in the presence of excess sulfur in a N_2-filled glovebox. It was found that small excesses of sulfur (~0.05 g) formed disconnected $BaZrS_3$ crystals, while higher amounts of sulfur (> 0.1 g) displayed continuous and large-grained surface morphologies (Fig. 14(a,b)). According to film XRD patterns, all peaks were assigned to $BaZrS_3$ (Fig. 14(c)). The film is still suffering from a two-layer structure, as seen in the cross-sectional SEM image.

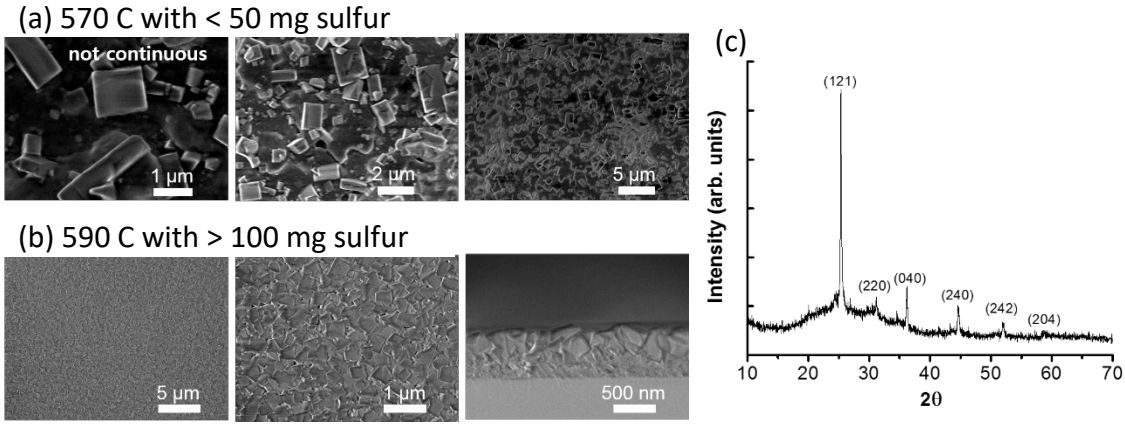

Figure 14. *SEM images of $BaZrS_3$ films grown (a) at 570 °C with < 0.05 g sulfur and (b) at 590 °C with > 0.1 g sulfur. XRD pattern of the $BaZrS_3$ film grown at 590 °C with > 0.1 g sulfur (c).*

To evaluate the optical properties of $BaZrS_3$, the absorbance and photoluminescence of the films were measured by UV-visible and PL spectroscopies (Fig. 15). The measured direct band gap of the films was found to be 1.89 eV. The PL spectra shows a broad peak with a maximum at ~690 nm, corresponding to 1.79 eV, consistent with the band gap. This band gap value implies potential for $BaZrS_3$ as a lead-free, air-stable semiconductor.

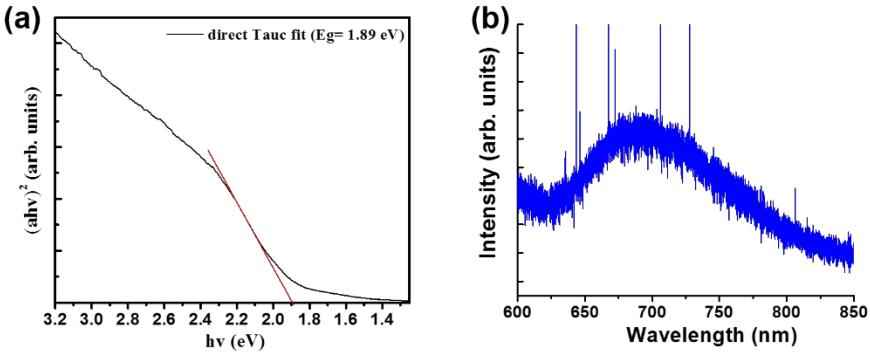

Figure 15. *(a) Tauc plot of absorbance data for a $BaZrS_3$ film assuming a direct band gap and (b) photoluminescence spectrum of $BaZrS_3$ film obtained using a 442 nm laser excitation source.*

Task 9: Defect physics in Pb-free down-selected materials

In this Task, the defect energy levels and formation energies in the Pb-free chalcogenide perovskite $BaZrS_3$ and the halide double perovskite $Cs_2AgBiBr_6$ have been calculated.

Defects properties of $BaZrS_3$: The performance of solar cells depends critically on the absorber defect properties. To optimize the performance, it is important to find growth conditions that suppress the formation of the unwanted deep level defects and promote the desirable beneficial defects. We have considered all twelve possible intrinsic point defects in $BaZrS_3$, including vacancies (V_{Ba}, V_{Zr}, V_S), interstitials (Ba_i, Zr_i, S_i), cation substitutions (Ba_{Zr}, Zr_{Ba}), and antisite substitutions (Ba_S, Zr_S, S_{Ba}, and S_{Zr}). The calculated transition energies of these point defects appear in Figure 16(a). It is noted that five defects (S_i, S_{Zr}, S_{Ba}, Zr_i and Zr_S) produce deep levels while other point defects produce shallow levels. For some defects with multiple charge states, the transition energy levels do not show trends. For example, for Zr_i, the (3+/4+) level is shallower than (0/1+) and (1+/2+) levels. We found that the lack of clear trends for these defects are due to the significant structural relaxation caused by multiple charge transfer.

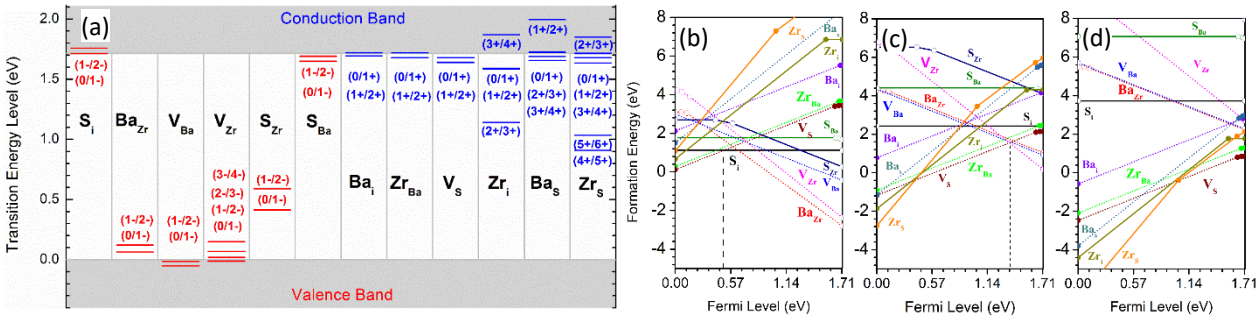

Figure 16. *(a) Calculated transition energy levels of intrinsic defects in $BaZrS_3$. The red bars show the acceptor levels and the blues bars show the donor levels. (b-d) Calculated formation energies of intrinsic point defects as a function of Fermi level at three representative chemical potential points: (b) A(S-rich/Zr-poor), (c) B (moderate), and (d) C(S-poor/Zr-rich).*[B]

We calculated the formation energies of the above point defects as a function of Fermi level position at three representative chemical potential points—A(S-rich/Zr-poor), B(moderate), and C(S-poor/Zr-rich) (Fig. 16(b-d)). Lines with open circle stand for acceptors, while lines with solid circles are for donors. Deep level defects are shown as solid lines, while dashed lines show shallow level defects. At chemical potential point B, the Fermi level position is pinned at 0.50 eV above the VBM by the formation of V_S and S_i, indicating that a weak *p*-type material can be grown. At chemical potential point C, the Fermi level position is pinned at 0.33 eV below the CBM by the formation of V_S and V_{Zr}, indicating the growth of *n*-type material. At chemical potential point D, the Fermi level position is pinned above the CBM, indicating degenerate *n*-type conductivity. Therefore, $BaZrS_3$ perovskite films grown under conditions towards S-poor/Zr-rich are expected to be *n*-type. Our results suggest that moderate growth conditions are desirable to synthesize $BaZrS_3$ perovskite absorbers for suppressed formation of deep level defects.

Defect properties of double perovskites $Cs_2AgBiBr_6$: We considered 20 intrinsic point defects, including vacancies (V_{Cs}, V_{Ag}, V_{Bi}, V_{Br}), interstitials (Cs_i, Ag_i, Bi_i, Br_i), and cation-on-cation (Cs_{Ag}, Cs_{Bi}, Ag_{Cs}, Ag_{Bi}, Bi_{Cs}, Bi_{Ag}), cation-on-anion (Cs_{Br}, Ag_{Br}, Bi_{Br}) and anion-on-cation (Br_{Cs}, Br_{Ag}, Br_{Bi}) antisites. Two representative chemical conditions are chosen at which the calculated defect formation enthalpies (ΔH) as a function of the Fermi level (E_F) are determined (Fig. 17(a,b)), along with an energy level summary (Fig. 17(c,d)).

The dominant defects Ag_{Bi}, V_{Bi}, and Br_i have deep transition levels in the bandgap, which would work as electron and hole traps and deteriorate the PV performance. It is found that all these deep defects can be significantly suppressed by synthesizing the material under Br-poor chemical conditions near the phase boundary between $Cs_2AgBiBr_6$, $Cs_3Bi_2Br_9$, and elemental Ag, where their ΔH values are at a maximum. Therefore, we propose that, to maximize the PV performance, growth of $Cs_2AgBiBr_6$ under Br-poor conditions will be preferred, if the precipitation of $Cs_3Bi_2Br_9$ and Ag can be avoided by kinetic barriers. This work has been published in *Chem Sus Chem.*[I]

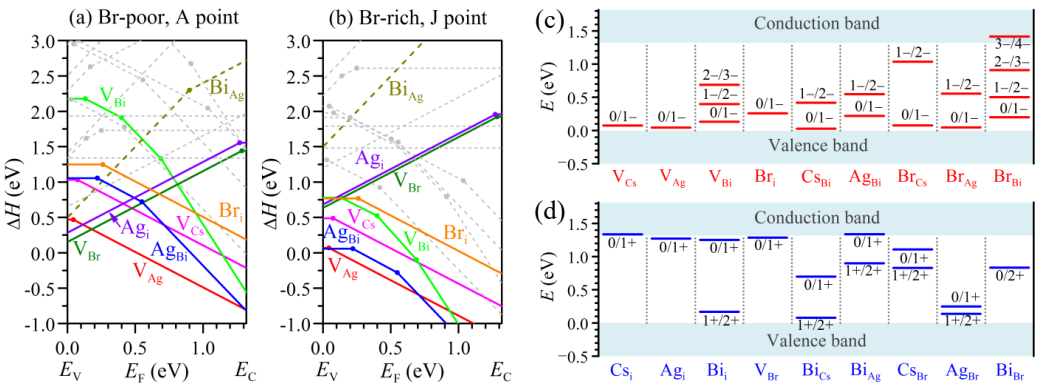

Figure 17. *Calculated formation enthalpies, ΔH, of intrinsic defects in $Cs_2AgBiBr_6$ as a function of the Fermi level, E_F, at two representative chemical potential points: (a) A (Bi-rich) and (b) J (Bi-poor). Defects with very high ΔH values are shown by the dashed lines. Calculated transition energy levels ε(q/q') for (c) intrinsic acceptors and (d) intrinsic donors in $Cs_2AgBiBr_6$.*[I]

Task 10 & 12: Photovoltaic devices with non-Pb and/or mixed anion perovskite layers and exploration of further Pb-free perovskite semiconductors

In Tasks 10/12 we explored various Pb-reduced and Pb-free perovskites for incorporation into PV devices including $(CH_3NH_3)_2PbI_2(SCN)_2$, $BaZrS_3$, $Cs_2Ag(Bi_{1-x}M_x)Br_6$ (M = In, Sb), and bismuth iodide materials $M_3Bi_2I_9$ (M = Rb, Cs) and $AgBiI_4$ through thin-film deposition and solid-state studies.

Two-dimensional perovskite $(CH_3NH_3)_2PbI_2(SCN)_2$: As previously discussed, $(CH_3NH_3)_2PbI_2(SCN)_2$ is an interesting PV candidate because: (1) the bandgap is suitable for solar cells application,[26] (2) the moisture stability is reportedly enhanced over $MAPbI_3$,[27] and (3) the band structure showed remarkably dispersive bands masses.[28] The original article also reported a working device with efficiency above 8% based on $(CH_3NH_3)_2PbI_2(SCN)_2$ as the absorber.[27] Encouraged by these findings, and from the fact that the layered structure of $(CH_3NH_3)_2PbI_2(SCN)_2$ may allow more flexibility for the replacement of toxic Pb with Sn, Sb or Bi, we focused on reproducing the data on $(CH_3NH_3)_2PbI_2(SCN)_2$ and making new Pb-free analogs of this compound.

We started with fabricating the devices made of already known compound $(CH_3NH_3)_2PbI_2(SCN)_2$. The precursor solution was prepared by dissolving stoichiometric CH_3NH_3I and $Pb(SCN)_2$ in DMF at room temperature, spin-coating on mp-TiO_2 using a typical solvent-engineering method. We immediately noticed that our films were red in color, which is in contrast with the expected color for a material with 1.6 eV band gap.

The UV-Vis spectroscopy measurements on our films showed that the actual band gap of the material is ~2 eV, consistent with the red color of the films (Fig. 18(a)).

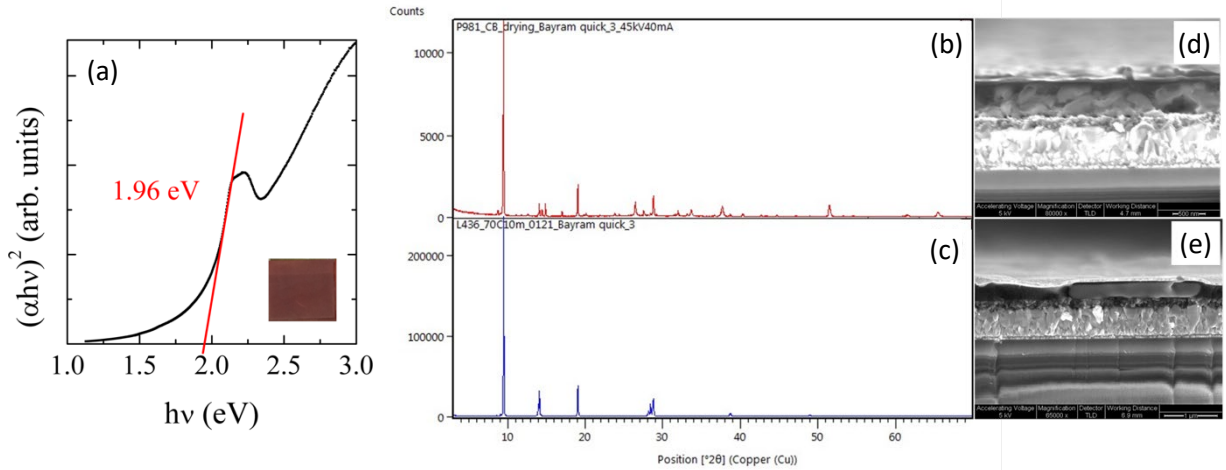

Figure 18. *(a) Tauc fit of the absorbance data assuming a direct band gap for $(CH_3NH_3)_2PbI_2(SCN)_2$ yields a 1.96 eV gap (inset shows the top surface of a corresponding thin film). X-ray diffraction pattern of films (b) before thermal annealing and (c) after thermal annealing; (d) and (e) are the corresponding cross-sectional SEM images, respectively.*

A post-deposition heat treatment at 70 ˚C for 10 minutes greatly increases the crystallinity of the films (Fig. 18(b)), preferably orients the grains, and aids in grain growth (Fig. 18(c)). From the cross-section images of the full devices, the $(CH_3NH_3)_2PbI_2(SCN)_2$ absorber, sandwiched by the HTL (Spiro-MeOTAD) and ETL (TiO_2), showed large grains across the film thickness after the annealing (Fig. 18(e)). Our devices based on such structures give the best efficiency of 2% (V_{oc} = 0.674V, J_{sc}= 4.69 mA/cm^2 and FF=0.68). The limitation of J_{sc} could be attributed to the large band gap of $(CH_3NH_3)_2PbI_2(SCN)_2$, and the oriented nature of our films. Given the 2D nature of $(CH_3NH_3)_2PbI_2(SCN)_2$, anisotropy in transport properties is expected for this material, and although the published band structure for this material suggests dispersive bands,[28] our work indicates that not all crystallographic directions were considered.[E]

In summary, we found several inaccurate reports in the literature regarding the properties of the layered perovskite $(CH_3NH_3)_2PbI_2(SCN)_2$, including the discrepancies in color, band gap, dispersions of bands around the Fermi level, stability and the performances of devices based on $(CH_3NH_3)_2PbI_2(SCN)_2$. In fact, the >8% devices reported in literature based on this material seems to include $CH_3NH_3PbI_3$ impurities.[27] We have reported our results in the *Journal of Phyiscal Chemistry Letters*.[E]

<u>Thin-film deposition of the chalcogenide perovskite $BaZrS_3$</u>: Due to the encountered challenges in Task 8, thus far we only conducted preliminary device-related work on $BaZrS_3$. In the first step, we tested the suitability of FTO substrates for $BaZrS_3$-based devices. Our current film fabrication procedure involves a sulfurization step at 580-595 ºC for a complete conversion of the sputtered (BaS + Zr) precursors. Normally, on glass substrates, this procedure yields dark red/grey $BaZrS_3$ films. Using FTO substrates, we carried out our regular sulfurization-annealing procedure at 585 ºC for 30 minutes, which yielded a visibly inhomogeneous film (Fig. 19(a)). In addition to the expected grey areas, attributed to $BaZrS_3$, there were yellow regions on top of the FTO. To determine if an

undesired reaction between the FTO substrate and $BaZrS_3$ is taking place, we also sulfurized at 585 ºC for 60 minutes, which resulted in almost a completely yellow film on the FTO section of the substrate. Notably, the etched glass region maintained the dark red/grey color, clearly indicating that the unwanted reaction only occurs on the FTO. XRD measurements confirmed that the grey film on the etched glass region of the substrate contains $BaZrS_3$, whereas the yellow regions demonstrate emergence of several impurity peaks (likely oxides), indicating the difficulty of fabricating traditional perovskite device architectures based on $BaZrS_3$.

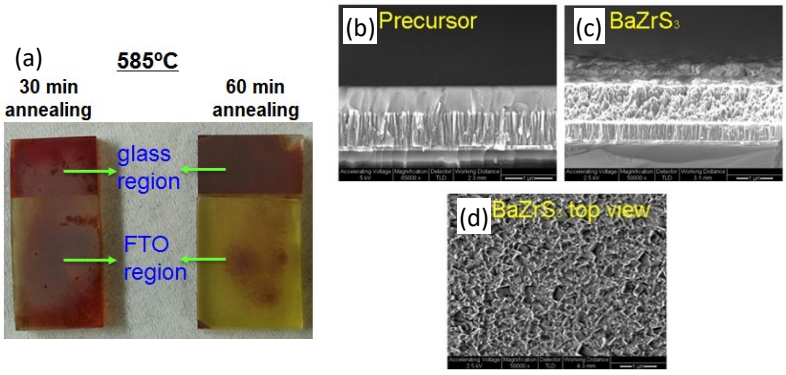

Figure 19. *(a) After sulfurization of $BaZrS_3$ precursors deposited on fluorine-doped tin oxide substrates at 585 ºC for 30 minutes and for 60 minutes. (b) As-sputtered precursor on a Mo-coated glass substrate. (c) After the sulfurization procedure at 585 ºC for 30 minutes, a thick (>500 nm) layer of MoS_2 is formed. (d) A top view of the sulfurized $BaZrS_3$ film.*

Next, we attempted to deposit $BaZrS_3$ on Mo-coated glass substrates, which have been successfully used for chalcogenide-based solar cell devices. Similar to that observed for chalcogenide-based devices such as Cu_2ZnSnS_4, however, during the sulfurization step, the Mo substrate reacts with S vapor forming a thick MoS_2 layer (Fig. 19(b-d)). To prevent this formation, we lowered the annealing temperature and reduced the sulfurization time. Our experiments showed that annealing temperatures below 500 ˚C (30 minutes) do not yield $BaZrS_3$. Given the glass transition and a possible formation of thicker MoS_2 layers at higher temperatures, 585-595 ºC annealing temperatures were taken as optimal.

Although high quality thin-films of $BaZrS_3$ can be deposited on a variety of substrates, we have not successfully fabricated high performance PV devices with $BaZrS_3$ as the absorber. To determine the root of the issue, we evaluated the electrical properties of the thin-films by resistivity measurements using the transmission line method (TLM) (Fig. 20(a)). These measurements indicate that the bulk carrier concentration of the $BaZrS_3$ films is much closer to an intrinsic value of 10^{10} cm^{-3}, as compared to the 10^{22} cm^{-3} value estimated from the position of the Fermi level measured by photoelectron spectroscopy (UPS/IPES). In order to understand this discrepancy, scanning transmission electron microscopy (STEM) plus energy dispersive spectroscopy measurements (EDS) were completed on a representative $BaZrS_3$ film (Fig. 20(b)). These measurements showed that the "$BaZrS_3$" film was actually composed of two layers—a Ba-Zr-S layer and a Ba-Zr-Te-O layer (Te is assumed to come from the substrate as there are no other Te sources in the experiment). These measurements show that in the bottom layer little to no sulfur is included. In addition to the two-layer structure, there are oxidized layers between and

on top of the $BaZrS_3$ grains. This could explain the contrasting PES and TLM results. As a bulk measurement, TLM shows a very high resistance (intrinsic doping—10^{10} cm^{-3}) because the current is impeded by the oxidized layers. On the other hand, the PES measurement is surface sensitive, and the Fermi level could be pinned at the surface at a very high doping level (~10^{22} cm^{-3}).

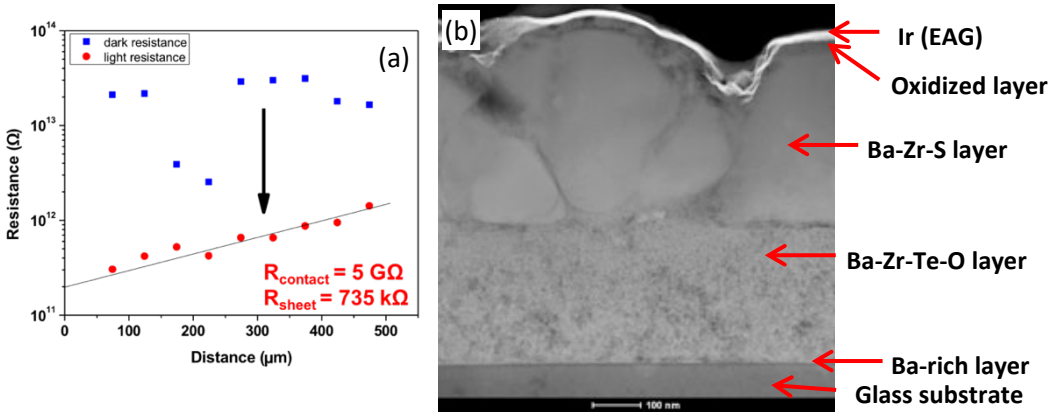

Figure 20. *(a) Resistance measurements in the dark (blue) and under white light illumination (red) and (b) high-angle annular dark field STEM micrograph on a comparable $BaZrS_3$ film.*

Halide double/triple perovskites $Cs_2Ag(Bi_{1-x}M_x)Br_6$ (M = In, Sb): Double perovskites have become a promising new candidate for optoelectronic application, but the bandgaps of the most known double perovskites are generally either large, indirect or direct forbidden—i.e., not suitable for high-efficiency PV application. Given these observations, further efforts focused on bandgap engineering are required if double perovskites are to play an important role in future optoelectronics. Using $Cs_2AgBiBr_6$ as host, we demonstrated bandgap engineering through additional alloying of In^{III}/Sb^{III} to form so-called "triple perovskites." $Cs_2Ag(Bi_{1-x}M_x)Br_6$ (M = In, Sb) accommodates up to 75% In^{III} with increased bandgap, and up to 37.5% Sb^{III} with reduced bandgap—i.e., enabling ~0.41 eV bandgap modulation, with smallest value of 1.86 eV for $Cs_2Ag(Bi_{0.625}Sb_{0.375})Br_6$. Associated band structure calculations, photoluminescence and environmental stability of the three-metal systems were also assessed.

At suitably small levels of In^{III} or Sb^{III} substituted into the Bi^{III} position of $Cs_2AgBiBr_6$, the products retain the original $Cs_2AgBiBr_6$ structure (Fig. 21(a)), as demonstrated with PXRD data (Fig. 21(b)). Increasing the level of substitution reduces the lattice parameter linearly following Vegard's law for both In^{III} and Sb^{III} incorporation (Fig. 21(c)). In addition, from Tauc plots for bandgap fitting based on UV-vis diffuse reflection data, we deduce direct bandgaps of from 2.15 eV to 2.41 eV and indirect bandgaps of from 1.86 eV to 2.27 eV in the $Cs_2Ag(Bi_{1-x}M_x)Br_6$ (M = In, Sb) alloys (Fig. 22). The bandgap of $Cs_2AgBi_{1-x}In_xBr_6$ increases from 2.12 eV to 2.27 eV as x increases from 0 to 0.75. In contrast, the bandgap of $Cs_2AgBi_{1-x}Sb_xBr_6$ decreases from 2.12 eV to 1.86 eV as *x* increases from 0 to 0.375 (Fig. 22(d)). The bandgap shift agrees with the sample color change (Fig. 22(e)). Further, all samples have relatively broad PL emission (Fig. 22(f,g)). For the In alloyed samples, large substitution suppresses PL intensity, with minimal change in peak position (Fig. 22(f)). For Sb-substituted samples, PL is quenched rapidly and obviously shifts to longer wavelength compared to the analogous spectrum for $Cs_2AgBiBr_6$ (Fig. 22(g)). While these

double perovskites tend to have bandgaps within reasonable energies for PV applications, the materials prove to be relatively unstable under ambient conditions. This work has been published in *Angewandte Chemie* and *ACS Energy Letters*.[O, R]

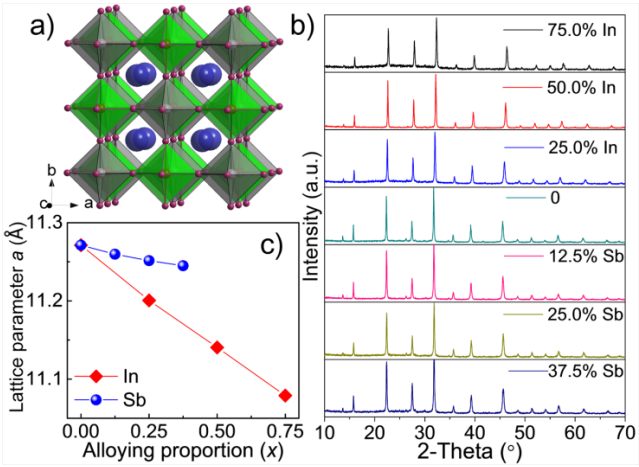

Figure 21. *The double perovskite structure shown in polyhedral representation (a), with grey, green, indigo and red spheres representing Ag, Bi, Cs and Br atoms, respectively. The PXRD of the compounds with different chemical substitutions (b); the variation of cubic crystal lattice parameter, a, as a function of substitution level, x, (c).*[O]

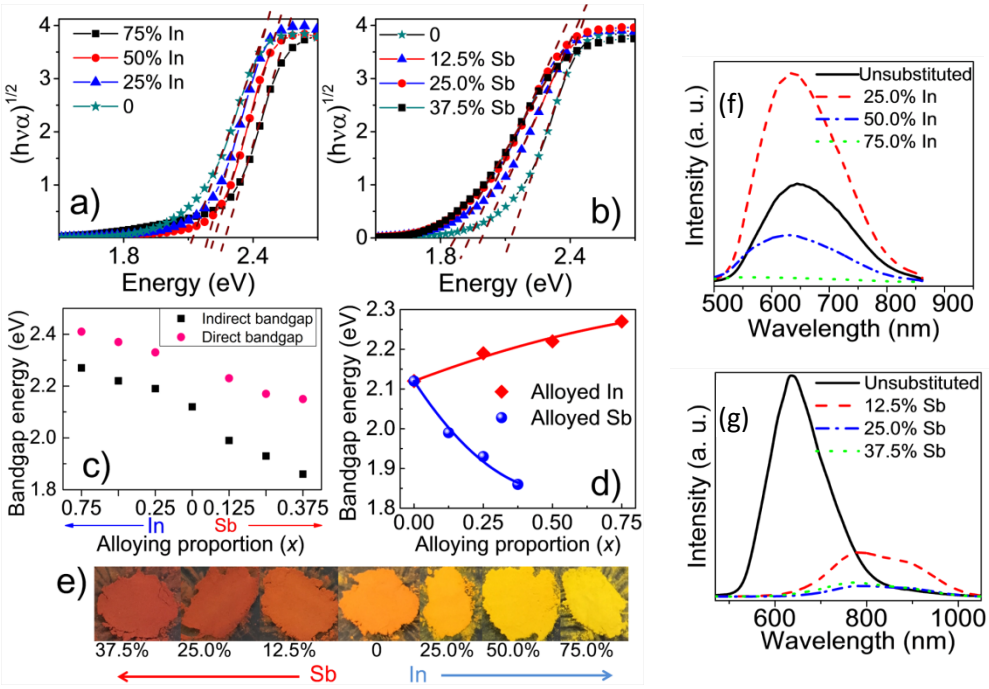

Figure 22. *The indirect Tauc plots of $Cs_2AgBi_{1-x}In_xBr_6$ (a) and $Cs_2AgBi_{1-x}Sb_xBr_6$ (b); apparent bandgaps of the compounds in this work extracted by linear fits to direct bandgap and indirect bandgap Tauc plots (c); a quadratic fit of the indirect bandgap as a function of In and Sb composition (x), respectively (d); photos of samples produced in this work (e). Overview of PL spectra for In-alloyed (f) and Sb-alloyed samples (g).*[O]

<u>Bismuth halide compounds $M_3Bi_2I_9$ (M = Rb, Cs) and $AgBiI_4$</u>: We have developed a two-step thin-film deposition approach for bismuth iodide materials $M_3Bi_2I_9$ (M = Rb, Cs) and $AgBiI_4$. Thermally co-evaporated precursor films are post annealed in an overpressure of BiI_3 in an N_2 filled glovebox. Smooth and pinhole-free films of $Cs_3Bi_2I_9$, $Rb_3Bi_2I_9$ and silver

bismuth iodide were fabricated (Fig. 23(a, b)). Direct band gaps of 2.2, 2.09 and 1.8 eV were obtained for $Cs_3Bi_2I_9$, $Rb_3Bi_2I_9$ and silver bismuth iodide, respectively (Fig. 23(c)).

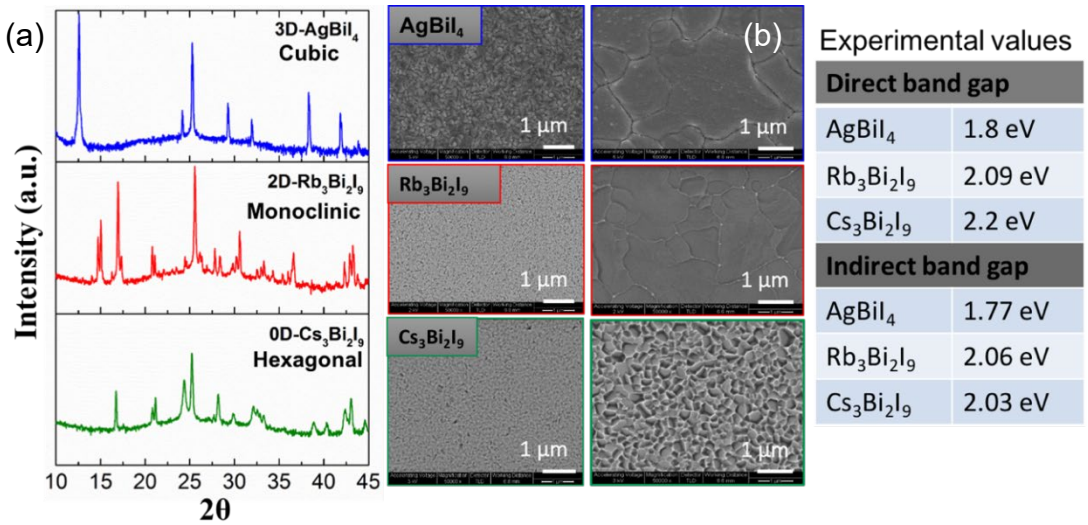

***Figure 23**. (a) XRD patterns of the as-deposited films of $AgBiI_4$ and $M_3Bi_2I_9$; SEM images of films before (b) and after (c) annealing; (d) optical band gaps of films determined by Tauc-plots of UV-vis spectra.*[W]

The ionization energy, Fermi level position and conduction band position were determined via XPS/UPS (in collaboration with Prof. Ian Hill's group at Dalhousie Univ.) to determine appropriate contact layer materials (Fig. 24(a)). For initial devices, TiO_2 and poly(3-hexylthiophene) (P3HT) were utilized in the devices as ETL/HTL, respectively. We have successfully fabricated PVs based upon the $AgBiI_4$ thin films (Fig. 24 (c)). A current density (J_{sc}) of 1.61 mA/cm^2, V_{oc} of 0.81 V, FF of 46.2%, and PCE of 0.6% were obtained from the best solar cells (Fig. 24(d)). In order to improve the performance of the devices, one possibility is to evaluate other HTLs with appropriately matched valence bands. This work has been reported in *Chemistry of Materials*[W] and *J. of Materials Chemistry A.*[Z]

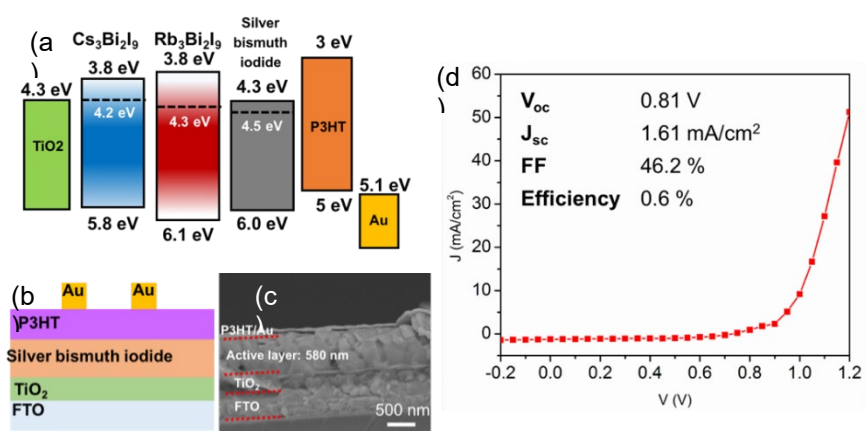

***Figure 24.** (a) Summary of the band positions of the $M_3Bi_2I_9$ (M = Cs, Rb) and $AgBiI_4$ thin films in relation to the proposed ETL, HTL and contact materials. (b) Schematic of the device structure based on $AgBiI_4$ films; (c) cross-sectional SEM image of device; (d) device JV characteristics.*

Task 11: High-performance device with inorganic hole transport layer (HTL)

In Task 11, several inorganic hole transport layers were explored for use in high-performing perovskite solar cells.

In order to optimize the inorganic HTL, we developed an inverted architecture for the perovskite solar cells, since deposition of an inorganic HTL on top of the perovskite absorber (in the conventional architecture) is prohibitively difficult owing to the aggressive processing methods used for most materials. Thus, the inverted architecture provides greater freedom of materials and processing conditions for the fabrication of the HTL, as deposition of the HTL occurs before the perovskite layer. The control architecture chosen for initial benchmarking consisted of the stack shown in Fig. 25(a), with the organic material PEDOT:PSS chosen as the reference. Using this architecture, devices with high fill factor, minimal hysteresis and a best PCE >13% (from J-V scans as in Fig. 25(d)) could be fabricated, indicating a well-behaved nature of the top contact stack (C_{60}/BCP/Ag) to be used for optimization of the inorganic HTL.

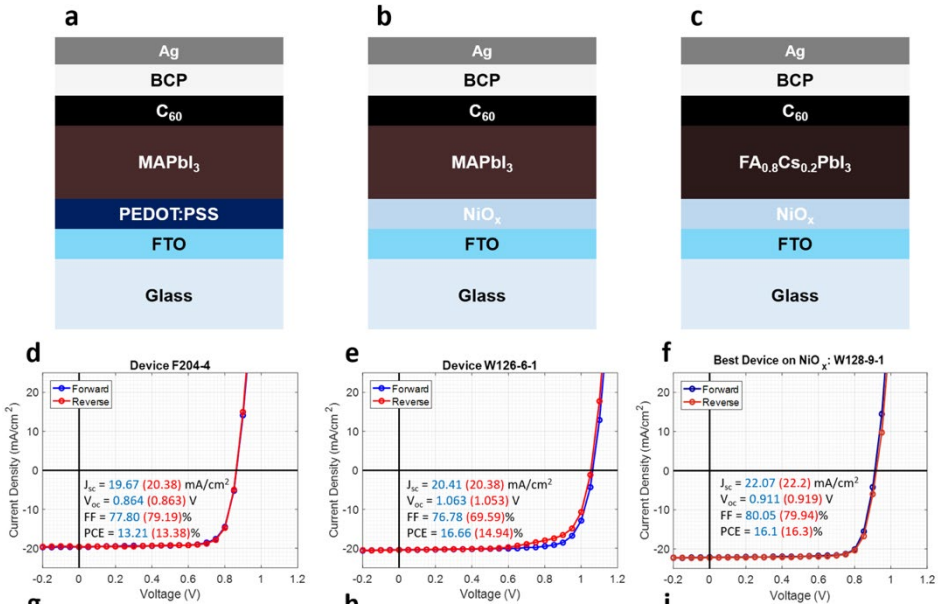

Figure 25. *Device architectures used for HTL optimization (a-c); J-V curves of best-performing devices of each type (d-f); stabilized power conversion efficiency of each type (g-i).*

To select a good HTL candidate, we conducted a literature review of materials with favorable properties and high performance in solar cells, including NiO_x, CuSCN, CuI, CuO_x, V_2O_5, CoO_x, WO_x, MoO_x, and delafossites such as $CuGaO_2$ and $CuCrO_2$. Based on its wide use for high-efficiency perovskite solar cells, we chose to focus on NiO_x as the primary HTL for initial device optimization. We have also pursued, in collaboration with the group of Prof. Julia Hsu at the University of Texas at Dallas, a study of devices based on the delafossite $CuCrO_2$, which had not yet been demonstrated as an HTL for PSCs but has favorable properties for a prospective HTL.

Using a spin-coating recipe from Prof. Franky So's group at North Carolina State University for deposition of NiO_x, we were immediately able to improve upon the PEDOT:PSS-based reference devices, primarily through improvement of the open-circuit voltage, yielding a best device in the initial batch with stabilized power conversion efficiency of over 15% (Fig. 25(d-f)). Further improvement upon this performance was achieved by adding 5 mol% $Pb(SCN)_2$ to the $MAPbI_3$ precursor solution, which on multiple occasions yielded devices with power conversion efficiency above 16% (best device J-V in Fig. 25(e)). Unfortunately, these devices tended to be unstable and yields of quality

devices in a batch were low. To improve device stability, we explored the mixed cation perovskite $FA_{0.8}Cs_{0.2}PbI_3$. Devices using this absorber proved both more reliable and higher-performing than the $MAPbI_3$ devices prepared with SCN, and yielded the highest-performing device so far produced by our group in the inverted architecture, with efficiency above 16% and a fill factor above 80% (Fig. 25(f)), validating NiO_x as a HTL.

We also investigated $CuCrO_2$ as an alternative HTL. Using ITO/$CuCrO_2$ films prepared by Prof. Julia Hsu's group at UT Dallas, devices were fabricated using the same top contact (C_{60}/BCP/Ag) as described above for the NiO_x work (Fig. 26(a)). Initial devices made with a sol-gel-deposited $CuCrO_2$ layer were limited by frequent electrical barriers, as the sol-gel process resulted in Cu-doped CrO_x, which should not be expected to work as an HTL. When $CuCrO_2$ nanoparticle suspensions were prepared by microwave-assisted hydrothermal reaction and spin-coated on the ITO substrates, $CuCrO_2$ films could be obtained, and the devices were free of the barrier behavior. The best devices so far prepared by this method demonstrate stabilized PCE above 12% (Fig. 26(b)), with low hysteresis and good agreement between the short-circuit current measured from J-V scans (Fig. 26(c)) and calculated from external quantum efficiency measurement (Fig. 26(d)). This work has been published in the *Journal of Materials Chemistry A.*[V]

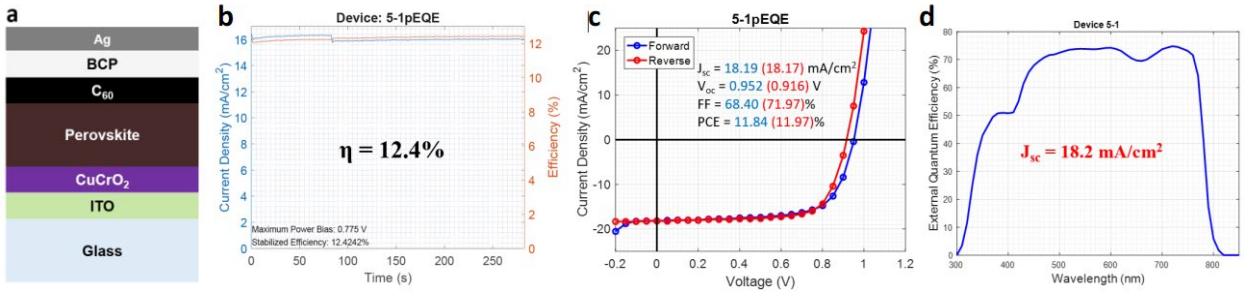

Figure 26. *Device architecture for optimization of $CuCrO_2$ devices (a). Stabilized efficiency (b), J-V scans (c), and external quantum efficiency (d) of the best-performing $CuCrO_2$ device.*[V]

Task 13: Calculating band offset between new absorbers and contact layers

In this task, we evaluated the suitability of three main methods for calculating the band offsets between two different semiconductors based on first-principles calculations and used this to calculate band offsets in delafossite materials. In addition, we introduced the importance of *electronic dimensionality* for PV properties of a certain material and used this knowledge in new calculations of the electronic properties of double perovskites and other halide perovskites.

Methods for calculated band offsets methods and application to delafossites: Before calculating the band offsets between contact materials and perovskites, we assessed three different techniques for calculating the offsets, including: (1) Branch point energy method, (2) Anderson's rule method, and (3) explicit interface modeling.

(1) Branch point energy method. The basic idea is that an interface dipole forms at an interface due to band discontinuities. This dipole depends on the band offset and tends to drive the band lineup towards zero-dipole condition. The branch point energy is universal on an energy scale and is the energy position where the character of electronic states changes from valence-band-like to conduction-band-like. Therefore, there is a

branch point energy level E_B for each semiconductor, as shown in Fig. 27(a). When the two semiconductors contact with each other, the branch point energy should be aligned. Then the band offset $\Delta E_C = \Delta_1 - \Delta_2$ can be obtained. The branch point energy E_B, which can be approximated as the effective mid-gap energy, can be calculated by:

$$E_B = \frac{1}{2}\sum_{\boldsymbol{k}}\left[\frac{1}{N_C}\sum_{i}^{N_C} E_{C_i}(\boldsymbol{k})w_{\boldsymbol{k}} + \frac{1}{N_V}\sum_{i}^{N_V} E_{V_i}(\boldsymbol{k})w_{\boldsymbol{k}}\right]$$

The subscript C and V denote conduction bands and valence bands, respectively. E is the band energy and *w* is the weight of the ***k*** point. N is the number of bands.

(2) The Anderson's rule (or the electron affinity rule) states that the vacuum levels of the two semiconductors on either side of the heterojunction should be aligned (Fig. 27(b)), where IP and EA stand for ionization potential and electron affinity, respectively. From the left panel of Figure 27(b), it is seen that $\Delta E_C = \Delta EA$ and $\Delta E_V = \Delta IP$. Thus, the main task is to calculate the IP and EA of each semiconductor. One can adopt a two-step recipe for this purpose—i.e., one bulk and one slab calculation (Fig. 27(b)). From the bulk calculation, we can obtain the CBM and VBM with respect to the average electrostatic potential (E_H). From the slab calculation, the offset between the vacuum level E_{vac} and E_H can be found. Then, the IP and EA can be calculated as $\Delta IP = \Delta - \Delta_1$ and $\Delta EA = \Delta - \Delta_2$.

(3) In the explicit interface modeling, one needs to construct a real interface between the two semiconductors. All the interface details, e.g. crystal orientation, bonding, defects, relaxation and strains are included in the modeling. To calculate the band offset, a three-step recipe is usually adopted, as shown in Figure 27(c). Two separate bulk calculations are performed to get the band edge positions with respect to a reference energy level, which can be some core levels or E_H. Another supercell calculation, which includes the interface, is used to calculate the offset of the two reference energy levels. Finally, the band offset can be obtained as $\Delta E_C = \Delta - \Delta_1 - \Delta_2$.

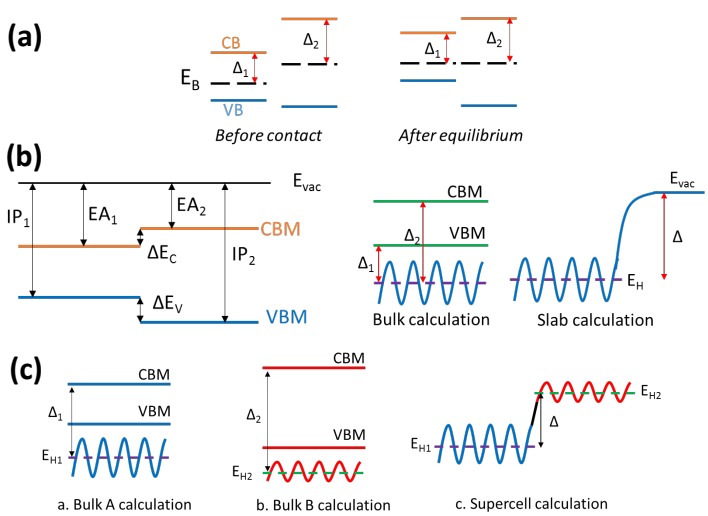

***Figure 27**. (a) Band diagram for alignment of the branch point energy. (b) Left panel: Band diagram shows the Anderson' rule. Right panel: The two-step recipe to calculate the IP and EA. (c) The three-step recipe to calculate the band offset by explicit interface modeling.*

For method 1, there is uncertainty about choosing the number of bands to average. For method 3, specific crystal orientation and small lattice mismatch are required to get reasonable results. Thus, we choose method 2 to calculate the band offset between new absorbers and electron and hole transporting layers.

We calculated the band structures and the excitonic properties of delafossites $CuMO_2$ (M = Al, Ga, In, Sc, Y and Cr) by using a state-of-the-art *GW*-BSE approach. The HSE wave functions were used as the starting point of the *GW* calculations for $CuCrO_2$, since HSE corrects the band orders wrongly predicted by PBE. For other delafossites, PBE wave functions were employed. Our results show that all of the delafossites are indirect band gap semiconductors with large exciton binding energies, varying from 0.24 to 0.44 eV. The lowest and strongest exciton absorption is always located at the L point of the rhombohedral Brillouin zone, mainly contributed from either Cu 3*d* → Cu3*p* (Al, Ga, In) or Cu 3*d* → M 3*d* (M = Sc, Y, Cr) transitions. Taking the electron-hole effect into account, the calculated band gaps agree quite well with experimental values.

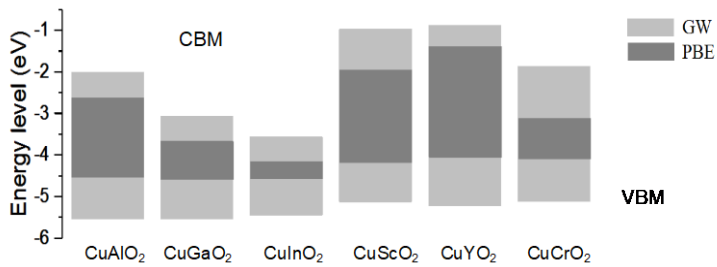

***Figure 28**. Band alignment of the Cu-based delafossites. Dark and light gray rectangles show the PBE and GW results, respectively. The top and bottom borders of the rectangles denote the positions of conduction band minimum (CBM) and valence band maximum (VBM), respectively.*

The GW method corrects the PBE bands by shifting the conduction and valence bands up and down, respectively, resulting in improved description of the band structures of Cu-based delafossites. Based on the calculated IP, the delafossites can be divided into two groups. The group IIIA delafossites ($CuAlO_2$, $CuGaO_2$, and $CuInO_2$) have relative larger IP of ~5.5 eV, while smaller IPs of ~5.1 eV are found for transition metal based delafossites ($CuScO_2$, $CuYO_2$, $CuCrO_2$). The band gaps of the latter are larger than those of the former. The band offset, calculated using the IP method, is shown in Figure 28. It has been reported that $CuGaO_2$ is a suitable HTL for $MAPbI_3$ perovskite solar cells. Therefore, the group IIIA delafossites are candidates as HTL for iodide perovskites, whereas, transition metal based delafossites may be more suitable HTL materials for bromides and chlorides. This work was published in the *Journal of Applied Physics.*[Q]

Importance of electronic dimensionality: Additionally, we introduced, for the first time, the concept of *electronic dimensionality* or the connectivity of the atomic-orbitals that comprise the lower conduction band and upper valence band. We showed that electronic dimensionality accounts for PV properties much better than structural dimensionality, with high electronic dimensionality providing the opportunity for (though not guaranteeing) high PV performance. Conventionally, structural dimensionality has been used as one metric to account for PV properties and device performances of absorbers. While this notion of structural dimensionality is successful for most absorbers, it fails for some others.

Figure 29 summarizes the experimental bandgaps and device performances of some metal iodide perovskites and non-perovskites. Most of the bandgap values of the materials correlate well with the structural dimensionality. These materials have the same structural and electronic dimensionality. To help understand the effects of structural and electronic dimensionality on the PV properties of perovskite materials, we show DFT calculated PV properties for prototype perovskite materials consisting of the same elements of Cs, Pb, and I, but different crystal dimensionalities, which consist of 3D networks, 2D monolayers and 1D single-chains of $[PbI_6]$ octahedra, and isolated $[PbI_6]$

octahedra (Fig. 29(c)). Figures 29(d,e) show the calculated band structures and optical absorption spectra of these materials, respectively. In each of these compounds (3D $CsPbI_3$, 2D Cs_2PbI_4, 1D Cs_3PbI_5, and 0D Cs_4PbI_6) the structural and electronic dimensionalities are the same—i.e. the orbitals at the CBM and VBM are connected along the same directions as the [PbI_6] octahedra. This leads to an easily seen trend that as the structural *and* electronic dimensionalities decrease, the band gap and effective masses increase because the hybridization of those orbitals decreases (Figs. 29(d,e)).

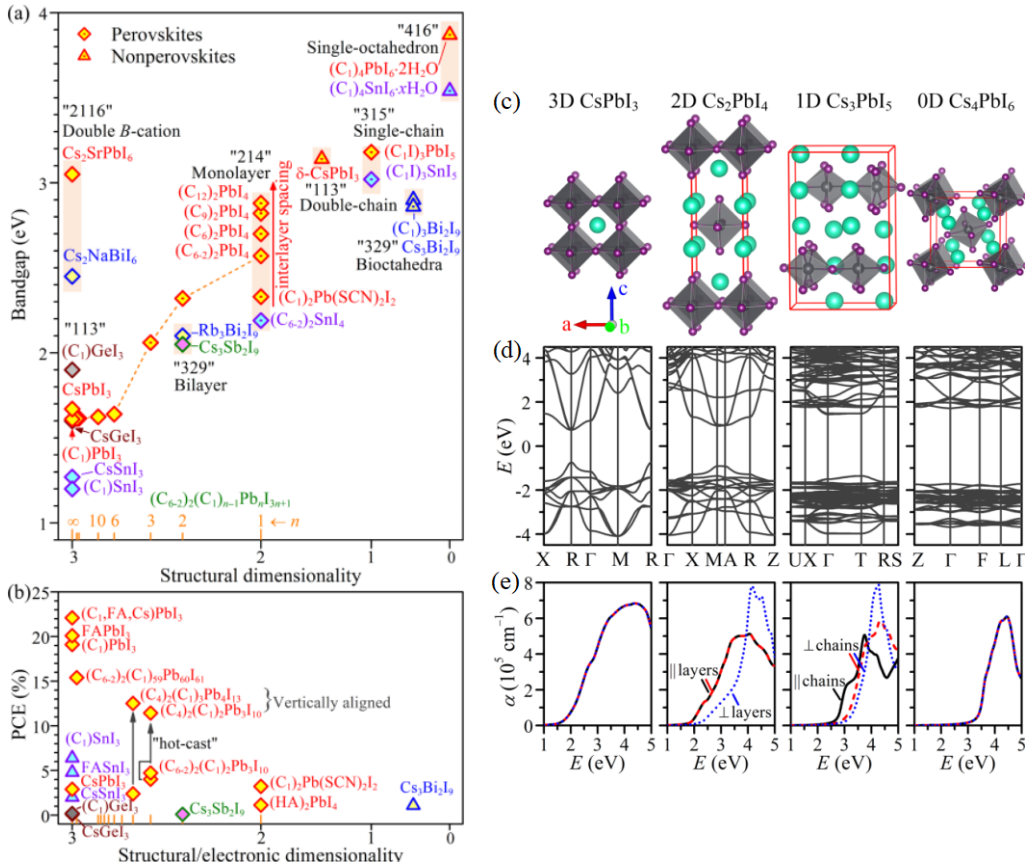

Figure 29. *(a) Experimental bandgaps of some iodide perovskites (diamonds) and non-perovskites (triangles) as a function of crystal dimensionality. For the dot-center symbols, optical bandgaps were determined by excluding the exciton band at low temperature. The structural dimensionality of an n-layered perovskite is defined as 3 – 1/n. (b) Highest recorded efficiencies for some iodide perovskite and non-perovskite absorber materials. "C_n" = $C_nH_{2n+1}NH_3$, "C_{6-2}" = $C_6H_5(CH_2)_2NH_3$, "C_1I" = $NH_2C(I)=NH_2$, "FA"= $HC(NH_2)_2$, and "HA" = $C_5N_3H_{11}$. (c) Hypothetical model crystal structures of $CsPbI_3$, Cs_2PbI_4, Cs_3PbI_5, and Cs_4PbI_6. (d) Calculated band structures and (e) optical absorption coefficients of model systems $CsPbI_3$, Cs_2PbI_4, Cs_3PbI_5, and Cs_4PbI_6.*[K]

The above materials exhibit the same structural and electronic dimensionality. Therefore, the bandgap trend, optical properties, and device performance can be explained well by the structural dimensionality. However, there are perovskites exhibiting electronic dimensionalities lower than their structural dimensionalities. For these perovskites, the trend of bandgap and optical properties can no longer be explained solely by the structural dimensionality; the electronic dimensionality must be considered. There are two major causes for lower electronic dimensionality: structural and chemical deviations.

The structural deviation is related to the rotation and/or distortion of [BX_6] octahedra. It is known that the bandgap of a perovskite can be affected by the structural distortion. Here, we show that the trend of the changes of PV properties caused by structural distortion can be qualitatively understood by the change of the electronic dimensionality. To understand this, we choose ideal 3D $CsPbI_3$ and 2D Cs_2PbI_4 perovskites as examples, in which all the Pb−I−Pb bond angles are 180°. For simplicity, we only change the in-plane Pb−I−Pb bond angle (denoted as θ in Fig. 30(a)) and maintain all Pb-I bond lengths as equal. Figure 30(b) summarizes the calculated bandgaps as a function of the in-plane Pb−I−Pb bond angle θ. As θ decreases from 180° to 136.4°, the bandgap of 3D $CsPbI_3$ increases slowly from 1.48 eV to 1.66 eV, while the bandgap of 2D Cs_2PbI_4 increases rapidly from 1.89 eV to 2.51 eV. This increase in bandgaps of both the 3D and 2D perovskites indicates a reduction in the electronic dimensionality due to decreasing hybridization of the orbitals in the bands.

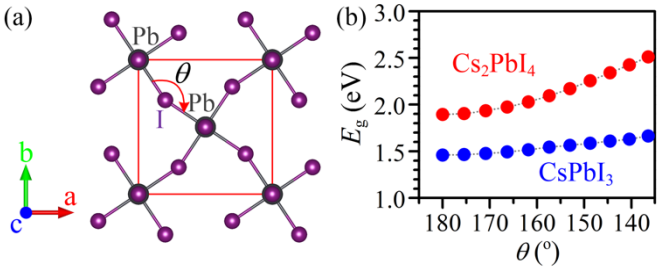

Figure 30. *(a) Schematic of Pb−I−Pb bond distortion in the ab plane of √2×√2-cells of $CsPbI_3$ and Cs_2PbI_4 perovskites. (b) Calculated bandgaps of $CsPbI_3$ and Cs_2PbI_4 perovskites as a function of the in-plane Pb−I−Pb bond angle θ.*[K]

To help understand how chemical deviations can lower the electronic dimensionality as compared to structural dimensionality, we calculate the band structure of a prototype double perovskite Cs_2SrPbI_6. This double perovskite is structurally 3D, but it has a bandgap significantly larger than the 3D single perovskites. Fig. 31(a) shows a 2 × 2 × 2 supercell of the 3D $CsPbI_3$ perovskite, which can be regarded as a nominal "double" perovskite of Cs_2PbPbI_6, which is isostructural to $Cs_2AgBiBr_6$. Cs_2SrPbI_6 is composed of a 3D octahedra network of alternatively-corner-shared [SrI_6] and [PbI_6] octahedra and, therefore, exhibits a 3D structural dimensionality. However, it should be noted that the [PbI_6] octahedra are isolated by the [SrI_6] analogues.

Figures 31(c,d) show the calculated band structures for Cs_2PbPbI_6 and Cs_2SrPbI_6. In each case the CBM and VBM are composed of mainly Pb atomic orbitals coming from the [PbI_6] octahedra. However, the nature of the band edges are very different. Cs_2PbPbI_6 resembles a normal single perovskite with dispersive bands, while Cs_2SrPbI_6 has relatively flat band edges. This character is very similar to a 0D perovskite, even though the double perovskite has a 3D structure. In Cs_2SrPbI_6, the [PbI_6] octahedra are electronically disconnected from one another, giving the double perovskite Cs_2SrPbI_6 effectively a 0D electronic dimensionality. The electronic dimensionality can also account for the device performances of perovskites and perovskite-alternatives listed in Fig. 29(b). When the structural dimensionality decreases to $2 \leq 3–1/n < 3$, the absorbers become layered perovskites, such as $(C_6H_{13}NH_3)_2(CH_3NH_3)_{n-1}Pb_nI_{3n+1}$, $(C_3H_7NH_3)_2(CH_3NH_3)_{n-1}Pb_nI_{3n+1}$, and $(C_4H_9NH_3)_2(CH_3NH_3)_{n-1}Pb_nI_{3n+1}$. Though these perovskites exhibit useful bandgaps and optical properties, the performances of devices based on randomly oriented films are much lower than those of the 3D $MAPbI_3$ and $FAPbI_3$ perovskites, since the photogenerated charges cannot effectively travel across the gap between the

inorganic layers because of the lower electronic dimensionality. The concept of electronic dimensionality and its impact on perovskites is published in *Materials Horizons*.[K]

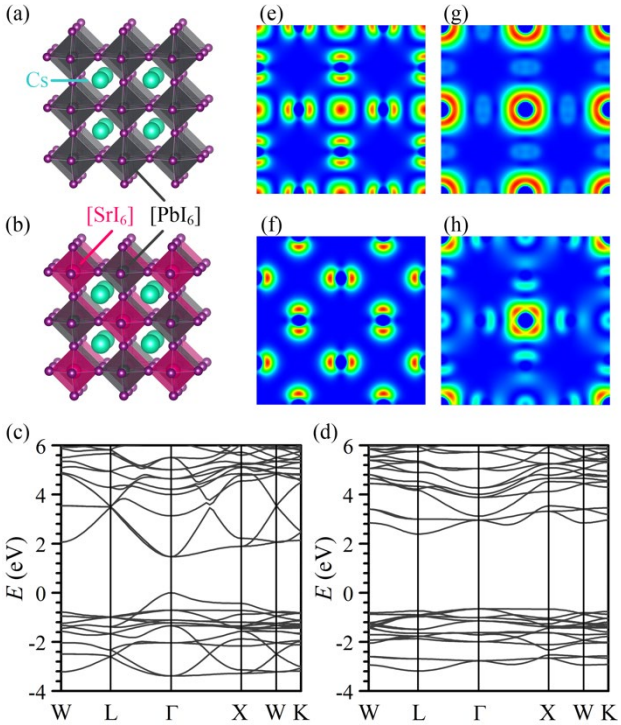

Figure 31. *(a,b) Crystal structures, (c,d) band structures, (e,f) VBM- and (g,h) CBM-associated charge density maps on the (100) plane, of (a,c,e,g,) Cs_2PbPbI_6 and (b,d,f,h,) Cs_2SrPbI_6. In Figs. c,d, the relative VBM and CBM positions of Cs_2PbPbI_6 and Cs_2SrPbI_6 are aligned by matching core levels.*[K]

Optoelectronic properties of new perovskites: Recently, there has been substantial interest in developing double-B-cation halide perovskites, which hold the potential to overcome the toxicity and instability issues inherent within emerging lead halide-based solar absorber materials. Among all double perovskites investigated, In(I)-based $Cs_2InBiCl_6$ and $Cs_2InSbCl_6$ have been proposed as promising thin-film PV absorber candidates, with computational examination predicting suitable materials properties, including direct bandgap and small effective masses for both electrons and holes. Through DFT calculations, we found that reduction/oxidation (redox) reactions oxidize In(I) to In(III) and reduce Bi(III)/Sb(III) to metal, destabilizing the proposed In(I)-based double perovskites. The DFT calculations suggest that the In(I)-based halide double perovskites will decompose spontaneously into products involving In(III)-based ternary compounds such as $CsInI_4$, $Cs_3In_2Br_9$, $Cs_3In_2Cl_9$ (Fig. 32(a-f)). Solid-state synthesis efforts confirm the theoretically predicted difficulty for preparing these compounds; all attempted reactions do not form the desired double perovskite phases. Instead, they form In(III)-based ternary compounds, with part of the Bi^{3+}/Sb^{3+} being reduced to metal. Our theoretical/experimental results are published in *Journal of Physical Chemistry C.*[L]

Using DFT calculations, we analyzed the optical absorption properties of lead (Pb)-free metal halide perovskites ($AB^{2+}X_3$) and double perovskites ($AB^{+}B^{3+}X_6$) (A = Cs or monovalent organic ion, B^{2+} = non-Pb divalent metal, B^{+} = monovalent metal, B^{3+} = trivalent metal, X = halogen). We showed that, if B^{2+} is not Sn or Ge, Pb-free metal halide perovskites exhibit poor optical absorptions because of their indirect bandgap nature. Among the nine possible types of Pb-free metal halide double perovskites (Fig. 32(g)), six have direct bandgaps. Of these six types, four show inversion symmetry-induced parity-forbidden or weak transitions between band edges, making them not ideal for thin-

film solar cell application. Only one type of Pb-free double perovskite shows optical absorption and electronic properties suitable for solar cell applications, namely those with B^+ = In, Tl and B^{3+} = Sb, Bi. These results are published in the *Journal of Physical Chemistry Letters.*[N]

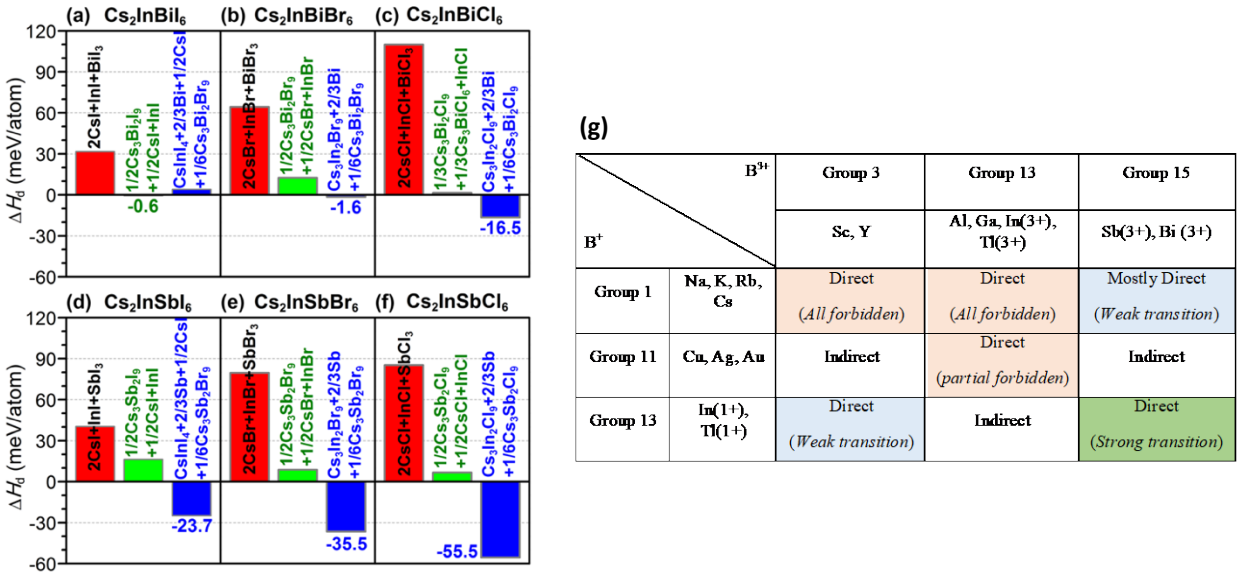

Figure 32. *Calculated decomposition energies (ΔH_d) of (a) Cs_2InBiI_6, (b) $Cs_2InBiBr_6$, (c) $Cs_2InBiCl_6$, (d) Cs_2InSbI_6, (e) $Cs_2InSbBr_6$, and (f) $Cs_2InSbCl_6$ along three representative decomposition pathways. The red bars indicate pathways involving only binary compounds. The green and blue bars indicate the lowest-ΔH_d nonredox and redox pathways involving ternary compounds. (g) Band gap type as a function of B^+ and B^{3+} metal choice, as determined by DFT-based analysis.*[L,N]

Task 14: Device stability assessment

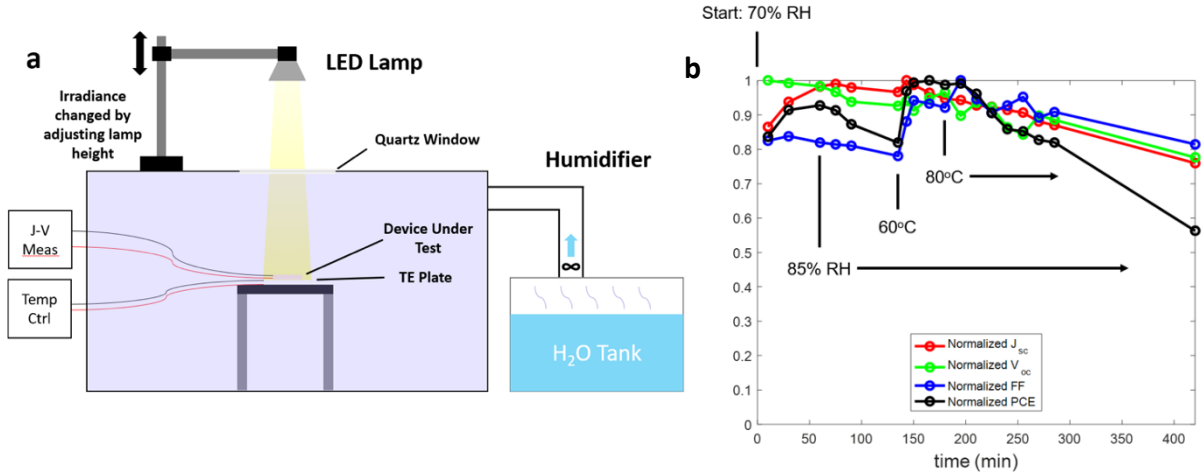

Figure 33. *Schematic of environmental testing chamber (a), and trends in device parameters during exposure testing of $FA_{0.8}Cs_{0.2}PbI_3$ solar cell (b).*

We completed a testing station for measuring device performance under conditions of elevated temperature and humidity using a modified environmental testing chamber from Electrotech Systems (Model 5503-1-11-600-0100). Relative humidity level control inside the box, from ambient to a maximum of 95%, is provided by a humidifier-hygrostat control

loop. Temperature control is achieved using a thermoelectric plate in contact with the device under test and may be set from ambient temperature to over 85°C. Device measurement consists of a white LED bulb approximating 1 sun (Sylvania 74052) whose irradiance is calibrated using a Newport Si reference cell, and feedthroughs to a Keithley 4200 sourcemeter for electrical characterization. A schematic of the testing station appears in Fig. 33(a). Performance of the testing station was validated by subjecting a reasonably high-performing (initial PCE ~15.75%) $FA_{0.8}Cs_{0.2}PbI_3$ solar cell to elevated temperature/humidity conditions. Device parameter degradation is shown in Fig. 33(b).

Task 15 & 16: Materials/device modeling, understanding and incorporation into preliminary photovoltaic devices

Under Task 15, multiple perovskite and perovskite-like compounds were investigated for solar cell applications. Theoretical/experimental studies were conducted in order to evaluate the potential of several materials, including $Cs_4CuSb_2Cl_{12}$-type systems, the chalcohalide $MASbSI_2$, monovalent In-based materials and Cs-Ti-Br-type compounds.

<u>$Cs_4CuSb_2Cl_{12}$-type semiconductor electronic properties and stability</u>: $Cs_4CuSb_2Cl_{12}$ has been reported as a new Pb-free layered perovskite (Fig. 34(a-d)) with a direct bandgap of 1.0 eV,[29] a suitable value for single-junction PV applications. However, the theoretical calculations presented in the paper showed that the Fermi level was in the valence band, a sign of metallic behavior. To understand this inconsistency and gain more insights into the optoelectronic properties of $Cs_4CuSb_2Cl_{12}$, we conducted DFT calculations and found that the magnetic ordering is of paramount importance in determining the fundamental properties of $Cs_4CuSb_2Cl_{12}$.

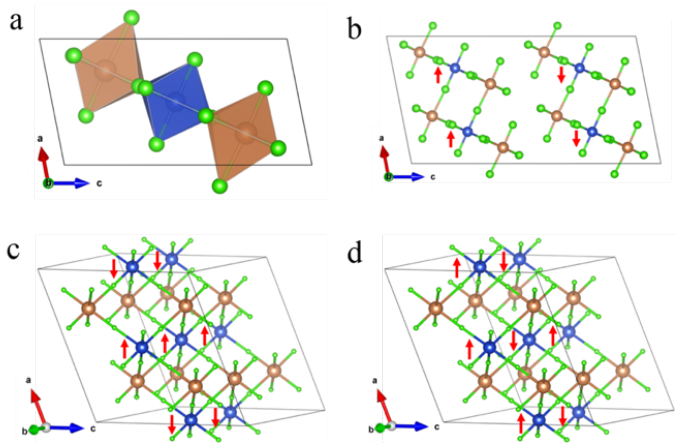

Figure 34. *(a) The primitive cell and (b)-(d) supercell with magnetic configurations of $Cs_4CuSb_2Cl_{12}$. The Cu, Sb, and Cl atoms are denoted by the blue, brown, and green balls, respectively. The voids between the octahedra are filled with Cs atoms, which are omitted for clarity. The red arrows denote the spin directions.*[S]

In $Cs_4CuSb_2Cl_{12}$, the oxidation state of Cu is +2; thus, there should be one unpaired electron in the Cu 3d orbitals. This unpaired 3d electron has spin freedom of up and down, which is responsible for a large magnetic moment at each Cu site. Different Cu sites with different spin states form different magnetic orderings, which change the electronic properties of $Cs_4CuSb_2Cl_{12}$ dramatically. We calculated the band structures of $Cs_4CuSb_2Cl_{12}$ with different magnetic orderings: paramagnetic (PM), ferromagnetic (FM), and anti-ferromagnetic (AFM). We employed PBE, PBE+U, and HSE functionals to treat the Cu 3d states. Although both PBE+U and HSE yield qualitatively correct band structures, PBE+U is superior to describe the band structures of Cu^{2+} compounds. By

comparing the total energies of all the configurations, we found the AFM-III is most stable. Figure 35 displays the PDOS of $Cs_4CuSb_2Cl_{12}$ in AFM configurations. The CBM is dominated by Cu 3d states. The Cu 3d→3d transitions are responsible for the small bandgap (~1.0 eV) of $Cs_4CuSb_2Cl_{12}$, as is shown in our published work in *arXiv*.[S]

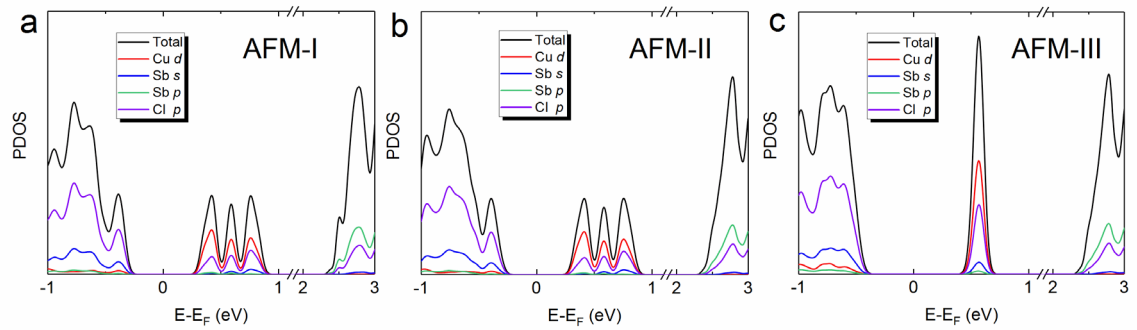

Figure 35. *PDOS of $Cs_4CuSb_2Cl_{12}$ in the antiferromagnetic configurations (a) AFM-I (b) AFM-II (c) AFM-III calculated from PBE+U.*[S]

Although the bandgap (~1 eV) of $Cs_4CuSb_2Cl_{12}$ is suitable for PV applications, the CBM is nearly flat, indicating poor carrier mobility. The lack of dispersion is due to the highly localized Cu 3d states. Therefore, we proposed $Cs_4SnSb_2X_{12}$ (X = Cl, Br, I) structures as alternatives to $Cs_4CuSb_2Cl_{12}$, wherein Sn has more delocalized p states. The PBE band structures of hypothetical $Cs_4SnSb_2X_{12}$ are shown in Figure 36. Both the valence and conduction bands of $Cs_4SnSb_2X_{12}$ are more dispersive than those in $Cs_4CuSb_2Cl_{12}$ due to the replacement of Cu by Sn. $Cs_4SnSb_2Cl_{12}$ and $Cs_4SnSb_2Br_{12}$ show indirect bandgaps of 1.8 eV and 1.5 eV, respectively, while $Cs_4SnSb_2I_{12}$ exhibits a smaller direct bandgap of 1.2 eV, from PBE calculations.

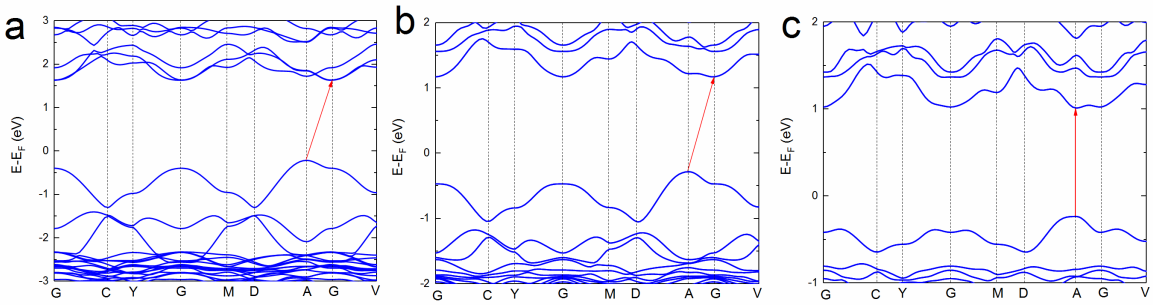

Figure 36. *PBE Band structures of (a) $Cs_4SnSb_2Cl_{12}$, (b) $Cs_4SnSb_2Br_{12}$, and (c) $Cs_4SnSb_2I_{12}$.*

For practical applications, we investigated the stability of the proposed $Cs_4SnSb_2X_{12}$. We considered the decomposition of $Cs_4SnSb_2X_{12}$ into $CsSnX_3$ and $Cs_3Sb_2X_9$ phases, which is the most probable reaction path. The decomposition energies of $Cs_4SnSb_2Cl_{12}$, $Cs_4SnSb_2Br_{12}$, and $Cs_4SnSb_2I_{12}$ are -0.025 eV, 0.040 eV, and -0.058 eV, respectively, per formula unit (pfu). Only $Cs_4SnSb_2Br_{12}$ is predicted to be stable against the decomposition reaction. However, $Cs_4SnSb_2Br_{12}$ has a large, indirect bandgap. To keep the direct bandgap feature of the $Cs_4SnSb_2X_{12}$ compounds, we replaced Cs with Rb and K to potentially stabilize the iodide compound. The decomposition energies of $Rb_4SnSb_2I_{12}$ and $K_4SnSb_2I_{12}$ with similar reaction path as above are 0.035 eV and 0.024

eV pfu, respectively. Therefore, both $Rb_4SnSb_2I_{12}$ and $K_4SnSb_2I_{12}$ are predicted to be stable against decomposition into the ternary phases. For binary phase decompositions, the decomposition energies are 0.26 eV and -0.08 eV pfu, respectively, for $Rb_4SnSb_2I_{12}$ and $K_4SnSb_2I_{12}$. $Rb_4SnSb_2I_{12}$ is stable against decomposition into binary phases. Based on our calculations, $Rb_4SnSb_2I_{12}$ could be a promising new Pb-free absorber.

Based upon the encouraging theoretical results, we pursued powder and single crystal syntheses for the $A_4SnSb_2X_{12}$-type compounds. Initially, we attempted to synthesize $Cs_4SnSb_2X_{12}$ powder samples by annealing the binary precursor compounds in an evacuated quartz ampoule. XRD patterns of the resulting reaction products are shown in Figure 37(a). In each of the patterns, the majority of the strongest reflections can be attributed to the $Cs_3Sb_2X_9$ and $CsSnX_3$ ternary decomposition products as labeled in Figure 37(a). This suggests that the Cs-Sn-based materials are not thermodynamically stable (consistent with the computational results).

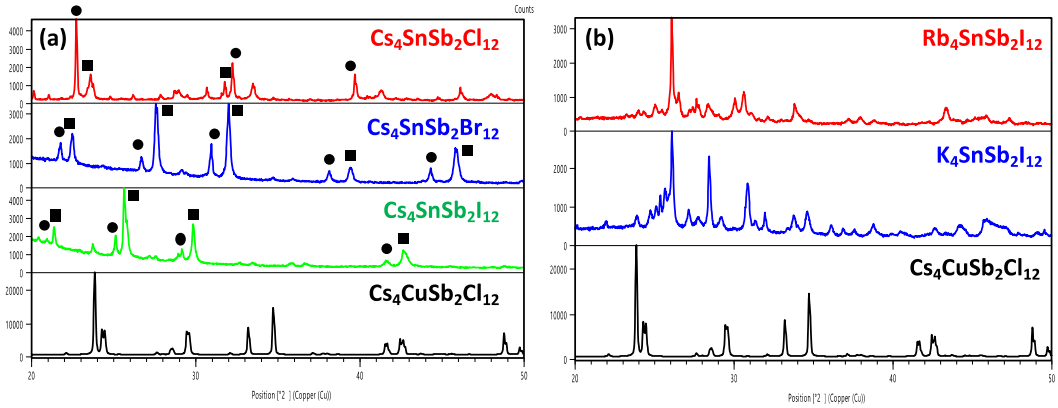

Figure 37. *XRD patterns of $Cs_4SnSb_2X_{12}$ mixtures with the targeted $Cs_4CuSb_2Cl_{12}$ reference pattern.*[29] *$Cs_3Sb_2X_9$ peaks are labelled with a square; $CsSnX_3$ peaks are labelled with a circle. XRD patterns (b) of $Rb_4SnSb_2I_{12}$ and $K_4SnSb_2I_{12}$.*

To target stable materials with a direct band gap, we replaced the Cs cation with Rb or K (in accordance with the computational results above). XRD patterns of powder samples of $Rb_4SnSb_2I_{12}$ and $K_4SnSb_2I_{12}$ synthesized from the binary iodide compounds are shown in Figure 37(b). The nominal $Rb_4SnSb_2I_{12}$ compound can be readily matched to the $Rb_3Sb_2I_9$ ternary decomposition phase. $Rb_3Sb_2I_9$ has been reported as a dark red compound, which matches the color of our powder. The $K_4SnSb_2I_{12}$ pattern cannot be assigned to any known binary or ternary decomposition phases, indicating that the quaternary compound may be the dominant phase within the sample, however a single crystal sample has yet to be synthesized for structural determination.

In summary, all $Cs_4CuSb_2Cl_{12}$-type compounds tested throughout this task tend to be thermodynamically unstable across various synthesis methods and temperatures. The reactions instead form various halide ternaries and binaries.

<u>Stability and electronic properties of $MASbSI_2$</u>: We studied the stability and electronic properties of the proposed 3D $MASbSI_2$ perovskite.[16] We assumed that the 3D $MASbSI_2$ perovskite is configured in a cubic phase with MA molecules aligned in an antiferroelectric configuration, which was found to be energetically more stable than other configurations, and sulfur atoms occupying the apical (along *z* axis) sites of the octahedra (Fig. 38(a)).

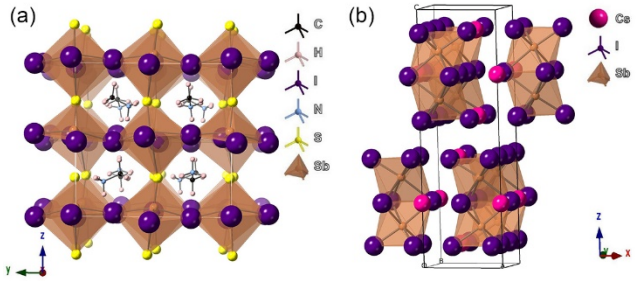

Figure 38. *(a) Proposed structure of $MASbSI_2$ from DFT relaxation and (b) crystal structure of $Cs_3Sb_2I_9$ as a representative member of the $A_3Sb_2I_9$ family.*[X]

To evaluate the thermodynamic stability of $MASbSI_2$, we considered the following two decomposition paths: (1) SbI_3, MAI, and Sb_2S_3 and (2) SbSI and MAI. The decomposition energy is defined as ΔE=E(products)-E(reactants). Negative ΔE indicates the instability of the reactant(s) with respect to the products. For the two pathways, the calculated ΔE is -1.00 eV/f.u. and -0.38 eV/f.u., respectively, indicating $MASbSI_2$ is unstable. Although the MA molecules are likely dynamically disordered, for the DFT calculations the dipole of the MA molecule must be situated in a specific direction. To examine the dipole interaction effects on the thermodynamic stability of $MASbSI_2$, we replaced the MA by the largest alkali metal, Fr. For $FrSbSI_2$, the calculated decomposition energy is -0.96 eV/f.u. and -0.36 eV/f.u, respectively. While reducing the magnitude of the negative decomposition energy slightly, the results suggest that the mixed sulfide and iodide perovskite is unstable (Fig. 39(a)).

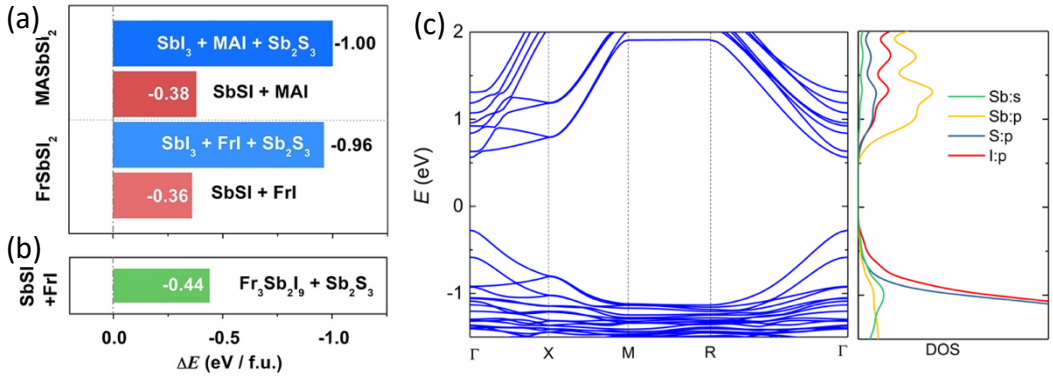

Figure 39. *Decomposition energies of different reaction pathways of (a) path 1 and 2 and (b) path 3 with Fr as the A cation. HSE06 band structure and DOS of the proposed $MASbSI_2$ (c).*[X]

Next, we investigated the energetics of the reaction to examine the likelihood of forming $MA_3Sb_2I_9$ from the results of the second decomposition path. For DFT calculations, similar to the case of $MASbSI_2$, we replaced the MA by Fr and evaluated the energetics of the described reaction. Total energy calculations showed that, with Fr replacement, the products are 0.44 eV/f.u. lower in energy than the reactants (Fig. 39(b)), which agrees with our experimental observation of the formation of $MA_3Sb_2I_9$ and Sb_2S_3.

While $MASbSI_2$ does not appear to be thermodynamically stable, this does not preclude the possibility of forming the phase under non-equilibrium conditions. To further understand the electronic properties of proposed $MASbSI_2$, its band structure and DOS were calculated based on the relaxed structure with HSE06 functional (Fig. 39(c)). The band structure diagram shows a 0.83 eV direct band gap, which is substantially smaller than the reported 2.0 eV.[16] The band edges are relatively dispersive in the vicinity of the

Γ point, pointing to good carrier mobilities. Overall, these characteristics indicate that such mixed sulfide/iodide phases could potentially be promising for PV applications.

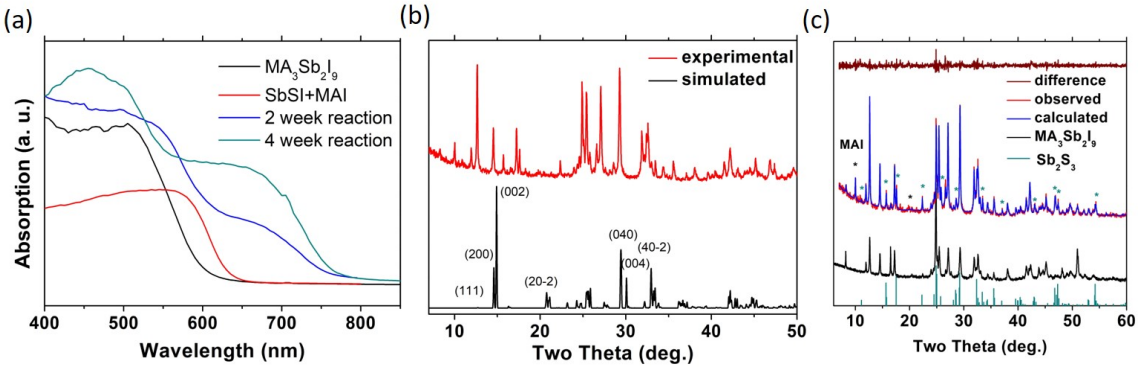

Figure 40. *(a) Absorption spectra of $MA_3Sb_2I_9$ and the SbSI + MAI reaction mixture before and during of the reaction at 160 °C, (b) comparison of measured XRD pattern of solid-state reaction product mixture and the simulated XRD pattern of $MASbSI_2$ based on the DFT-relaxed structure, and (c) Pawley profile fitting of the XRD pattern of the 160 °C solid-state reaction product to a mixture of MAI, $MA_3Sb_2I_9$ and Sb_2S_3. Peaks labeled by black asterisk are from MAI, and peaks labeled by green asterisk are from Sb_2S_3, black pattern is from $MA_3Sb_2I_9$ synthesized by solution methods, green stick pattern is from the Sb_2S_3 standard (PDF#42-1393).*[X]

To test the experimental stability of $MASbSI_2$, we annealed a pellet containing precursor materials in a sealed autoclave at 160 °C over a 4-week period and monitored the reaction progression via the color of the reaction product, XRD, and diffuse reflectance spectroscopy. With reaction progression, new absorption edges can be observed and there exist two distinct products in the reaction mixture (Fig. 40(a)), which can be identified as a red phase and grey phase. To confirm this composition of the solid-state reaction end-product, a fitting of the XRD pattern involving three phases, MAI, $MA_3Sb_2I_9$ and Sb_2S_3, was performed (Fig. 40(c)). All peaks in the observed pattern can be accounted for and the Pawley fit yields a very small difference curve between the observed and calculated patterns, suggesting that the reaction product mixture comprises these three phases with good confidence. This result indicates that the thermodynamically stable product of the reaction between MAI and SbSI should be $MA_3Sb_2I_9$ and Sb_2S_3 (contrary to the published report[16]). The experimental results confirm the computational predictions that this phase is not stable under thermodynamic equilibrium conditions. These combined results have been reported in the *Journal of Physical Chemistry Letters.*[X]

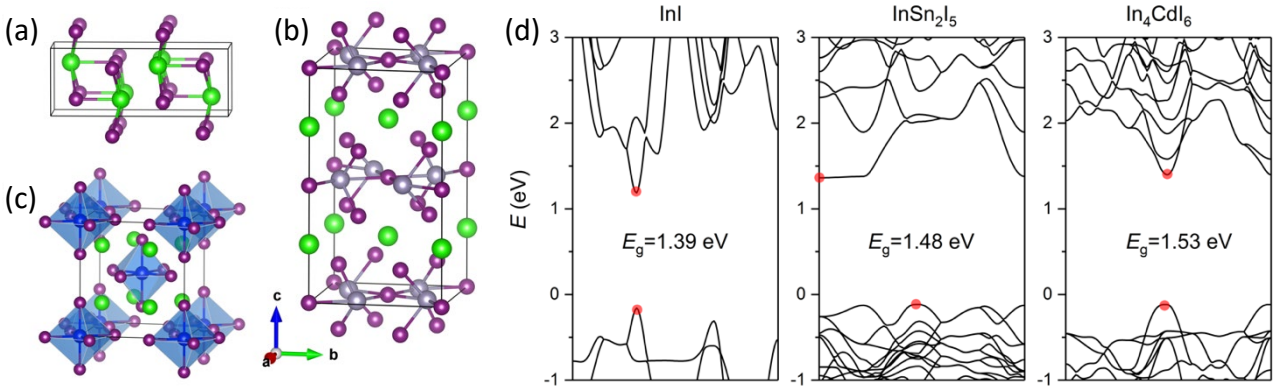

Figure 41. *Crystal structure of (a) InI, (b) $InSn_2I_5$ and (c) In_4CdI_6. Green, grey, blue and purple balls represent In, Sn, Cd and I, respectively. (d) Calculated PBE band structures of InI (left),*

$InSn_2I_5$ (middle) and In_4CdI_6 (right). D2 type van der Waals interaction correction is considered in all calculations. Red dots mark VBM and CBM.

<u>*Monovalent In-based semiconductors*</u>: Like Pb(II), In(I) also offers lone-pair s^2 electrons. Therefore, In(I)-containing compounds may exhibit PV-friendly electronic properties. We calculated the electronic properties of some experimentally reported In(I)-based systems, i.e., InI, $InSn_2I_5$ and In_4CdI_6, with crystal structures shown in Figures 41(a-c). In $InSn_2I_5$ and In_4CdI_6, In atoms have rather weak bonding with I atoms, behaving like the A cations in ABX_3 perovskite.

The calculated PBE band structures of the above three In(I)-based compounds appear in Figure 41(d). InI and In_4CdI_6 have direct bandgaps of 1.39 eV and 1.53 eV, respectively, with relatively dispersive band edges and bandgap. $InSn_2I_5$ has an indirect bandgap of 1.48 eV with a localized CBM.

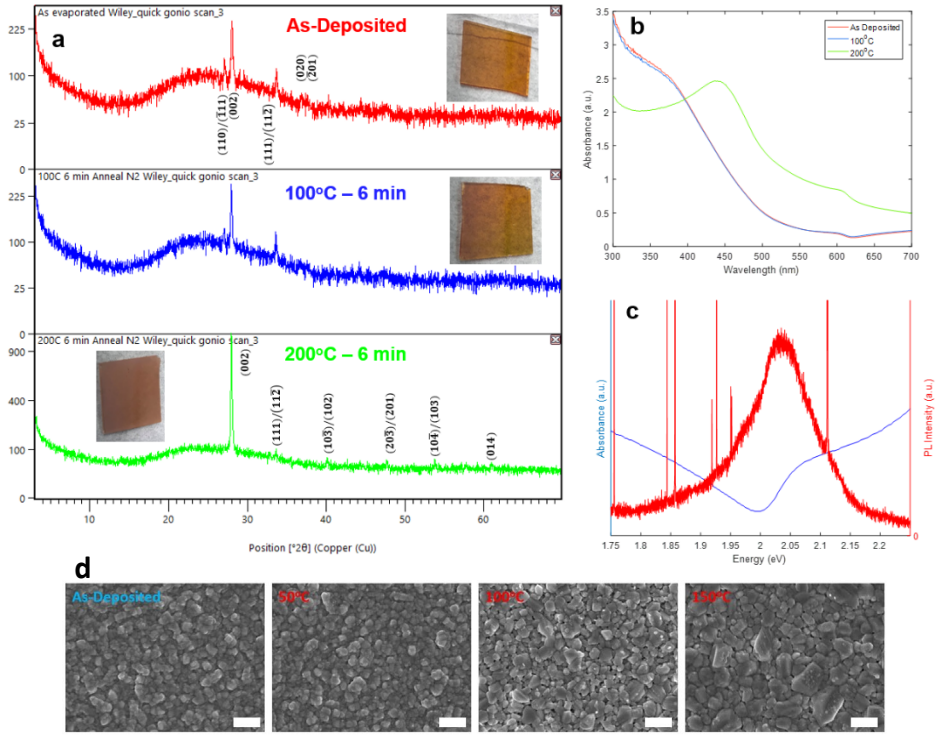

Figure 42. *XRD patterns (a) of InI films evaporated onto glass (film images, insets) and annealed at different temperatures; UV-Vis absorption of these films (b); comparison of the absorption and emission spectra in the vicinity of the band-to-band transition for as-deposited film (c). (d) SEM images of FTO/NiO_x/InI films annealed at different temperatures, demonstrating a tendency towards grain growth/pinhole formation with increasing temperature. Scale bars: 500 nm.*[AA]

Due to its chemical simplicity, potential for PV properties, and the fact that it serves as a precursor to the ternary indium halides, we first focused on depositing indium monoiodide. As In^+ can oxidize by interaction with solvents, we chose to focus on physical rather than solution deposition methods. We found that InI films could be prepared by thermal evaporation from a quartz crucible at temperatures ~200°C. As-deposited films on glass substrates were light brown, with a weak XRD (Fig. 42(a)). After post-annealing at 200°C the film surface changed from specular to matte, with nonuniformity suggestive of partial evaporation. Additionally, for the 200°C treated film, the (002) XRD peak became much more intense, indicating a preferred orientation along the c-axis (Fig. 42(a)). UV-vis

spectra show a direct band gap of ~2.0 eV (Fig. 42(b)). Weak band-to-band PL also arises when excited by a 442 nm He-Cd laser (Fig. 42(c)). SEM images of the as-deposited films reveal a close-packed film with small grain size (Fig. 42(d)). While there is no significant difference between the as-deposited film and the 50°C-annealed film, annealing the films at ≥100°C increases the grain size, but also leads to pinhole formation, thereby providing an explanation for the shunting behavior seen in the J-V curves of the initial device trials.

In order optimize the architecture of fabricated InI devices we performed UPS and IPES measurements on the evaporated InI films, and determine an IP, work function, and EA of 5.6 eV, 4.8 eV and 3.7 eV, respectively (Fig. 43(a, b)). These band positions also imply that device architectures commonly used for $MAPbI_3$ perovskite solar cells should also work well for InI, as the midgap energy is roughly the same for both materials, and the InI VB/CB are roughly 0.2 eV below/above the perovskite band edges. Concurrently with the UPS/IPES measurements, we have explored a device consisting of an ITO/CdS/InI/P3HT/Au stack (Fig. 43(c)). Overall, this architecture has proven more successful than the "inverted" devices fabricated, which showed strong current blocking characteristics. This optimized device architecture, combined with a SnI_2 treatment on the deposited InI films has led to the best efficiency currently attained using this structure—i.e., 0.44/0.38% as measured by J-V scan/stabilized photocurrent (Fig. 43(d)).

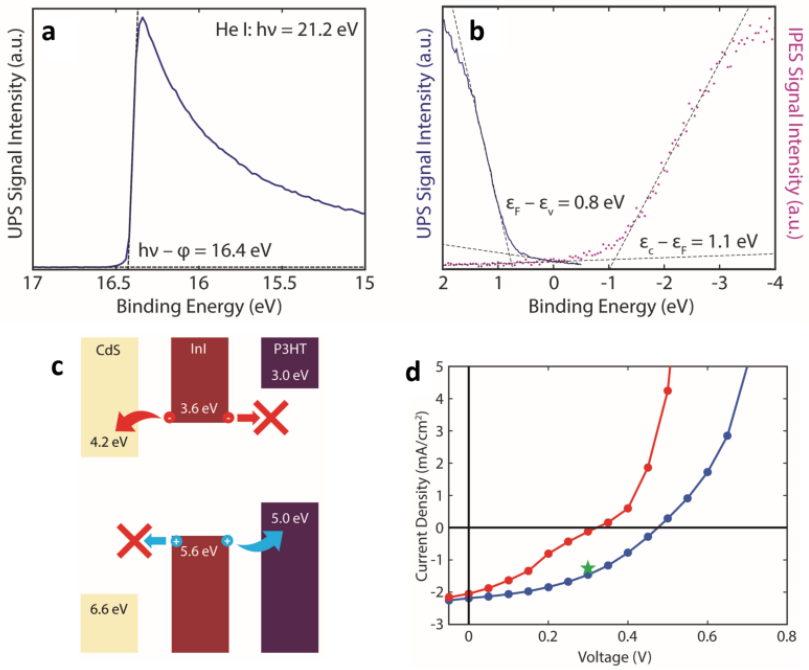

Figure 43. *(a,b) Photoelectron spectroscopy determination of the band positions and work function of InI; (c) band diagram of the most successful solar cell architecture, demonstrating that carriers are extracted and blocked by the ETL and HTL as desired; (d) forward (blue) and reverse scan (red) J–V curves and stabilized current/voltage at maximum power point (green star).*[AA]

The improvement in solar cell performance (from ~ 0.1% PCE) is most likely related to an influence of the SnI_2 treatment on the InI film composition. Biswas and Du have performed defect calculations and find that the Fermi level is likely to be pinned near midgap (~0.8 eV above the valence band) by Schottky defects, including iodine vacancies, which can contribute deep traps.[30] It is thought that the SnI_2 treatment satisfies at least some of the possible iodine vacancies in the InI films, thereby improving the device performance.

Finally, we evaluated the stability of the deposited InI films under ambient conditions. We exposed a freshly deposited film to ambient air (~50% relative humidity) and monitored its degradation visually, with XRD, and XPS (Fig. 44). Evidence of decomposition was visibly observable within 3 hours of exposing the film. The degradation spots eventually lost their color entirely and grew in size. No sign of decomposition was evident in XRD apart from a gradual lowering of the InI peaks, but higher binding-energy peaks in the In 3*d* and I 3*d* regions in the XPS spectrum of the aged film signify that oxidation occurs, with In_2O_3 and possibly iodine oxides or iodates as (amorphous) products. The implications are obvious and perfectly in line with expectations: the InI films are highly unstable in air, and therefore stringent precautions should be taken to avoid any interaction with ambient atmosphere whatsoever.

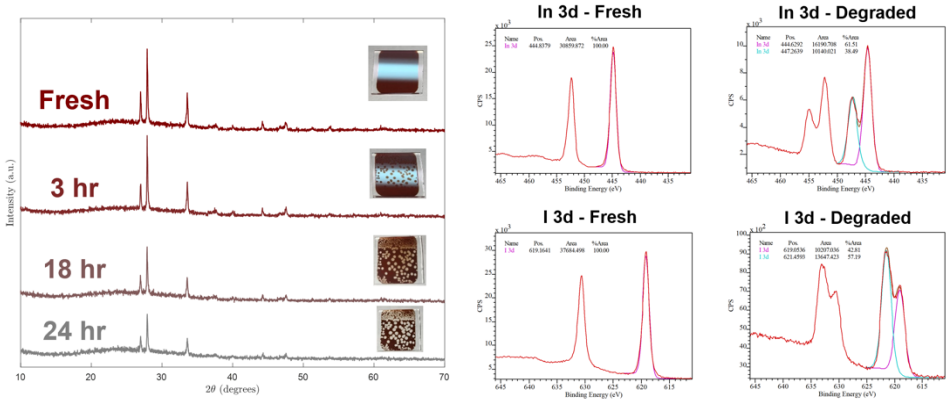

Figure 44. *Results of stability study on air-exposed InI films. XRD patterns do not indicate any obvious decomposition products, although the intensity of the InI peaks gradually fades. Additional higher binding energy peaks appear in the In and I XPS spectra of the degraded film, suggesting that both of these elements oxidize from environmental exposure.*

In summary, we have demonstrated that InI is a PV material, and explored the effect of the substrate on film properties and solar cell performance. Through UPS and IPES, we have established a device architecture that is conducive to hole and electron extraction and have attained a PCE of ~0.4%. However, the likelihood of deep traps in InI indicates that this material's potential PV performance may be limited. This work has been published in *Chemistry of Materials.*[Y]

<u>*Cs-Ti-Br compounds*</u>*:* Cs_2TiBr_6 emerged as a prospective Pb-free perovskite absorber following a report by Chen et al that suggested this material was stable under ambient conditions and had a strong PL signal.[31] Within Task 15/16, we have evaluated these claims both computationally and experimentally with the goal of developing high performing solar cells. However, as will be seen, this material has proven to readily degrade upon exposure to atmospheric conditions and does not have as promising optical properties as originally reported.

We evaluated the structural/electronic properties of various Cs-Ti-Br compounds using DFT calculations. Cs_2TiBr_6 with +4 Ti oxidation state has a vacancy ordered cubic perovskite structure (Fig. 45(a)). The [$TiBr_6$] octahedra are isolated, indicating low electronic dimensionality, as also demonstrated by the flat bands in the band structure (Fig. 45(d)). $Cs_3Ti_2Br_9$ has a hexagonal crystal structure (Fig. 45(b)) with isolated face-sharing [$TiBr_6$] octahedral dimers. The oxidation state of Ti is +3, so that there is only one

electron in the Ti *d* state, which makes $Cs_3Ti_2Br_9$ magnetic (ground state is found to be ferromagnetic). The band structure (Fig. 45(e)) provides an indirect bandgap from K to Γ. The PBE bandgap is 0.3 eV. $CsTiBr_3$ provides a 1D structure with face-sharing [$TiBr_6$] octahedral chains (Fig. 45(c)). The crystal structure is also hexagonal. The oxidation state of Ti is +2. $CsTiBr_3$ also leads to a ferromagnetic ground state. From the band structure, the bands cross the Fermi level along ΓA, meaning $CsTiBr_3$ is metallic (Fig. 45(f)).

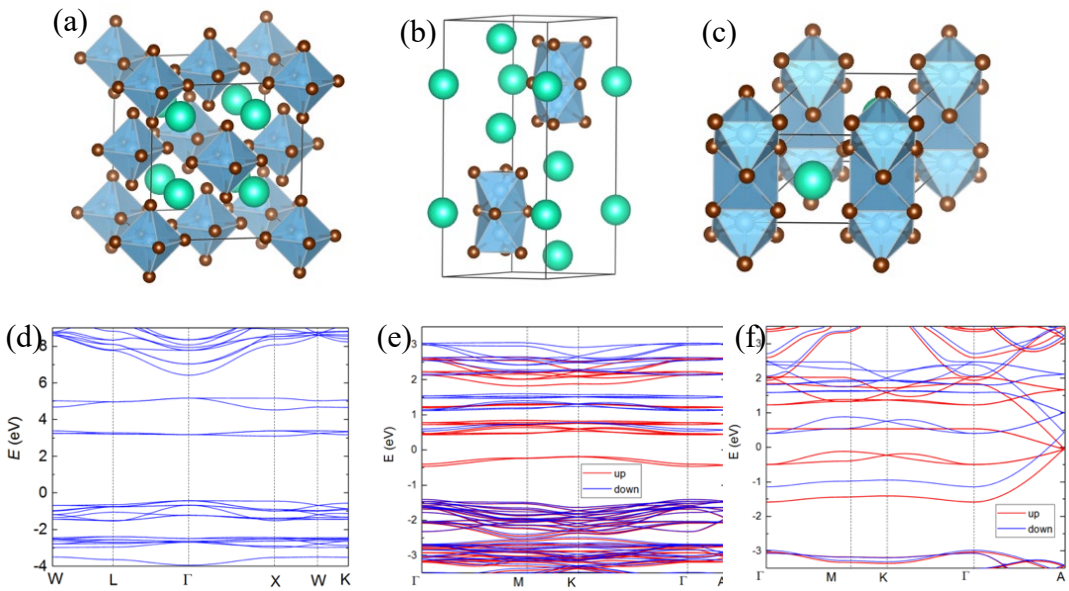

***Figure 45**. Crystal structures of (a) Cs_2TiBr_6, (b) $Cs_3Ti_2Br_9$, and (c) $CsTiBr_3$ and band structures of (d) Cs_2TiBr_6, (e) $Cs_3Ti_2Br_9$, and (f) $CsTiBr_3$.*

Based upon reported promising theoretical[32] and experimental[31] results on the Cs_2TiBr_6 perovskite for solar cell applications, we attempted to reproduce the film and powder data for this compound. We deposited the thin films by evaporating CsBr and then annealing these films in an excess of $TiBr_4$ under a glass cover in a glovebox. These first attempts led to an unstable material (Fig. 46). We tried to reproduce the film growth using an autoclave, as in the reported setup. The autoclave was heated in a furnace at 200°C for 48h. After heating, the system was opened in a glovebox, where the film was rinsed with toluene to remove the excess $TiBr_4$. XRD spectra of the resulting film, measured under Kapton to avoid the rapid degradation in air during the measurement, along with the corresponding spectrum for a film synthesized using our previous setup and the spectrum published by Chen et al. are shown in Figure 46(a). We obtain very similar spectra for both of the setups. We observe two peaks—(111) and (022)—that are not in the reference spectrum. To evaluate the stability of our layer in ambient atmosphere, we carried out XRD analysis over time after removing the protective Kapton film (Fig. 46(b)) and observe a rapid increase of the CsBr peak at 29° and a progressive decrease of the Cs_2TiBr_6 peaks. After 23 hours in ambient atmosphere, only CsBr peaks are observed in the XRD pattern. As a result, using an autoclave to grow the Cs_2TiBr_6 film by vapor annealing does not lead to a stable compound, contrary to the initial report.

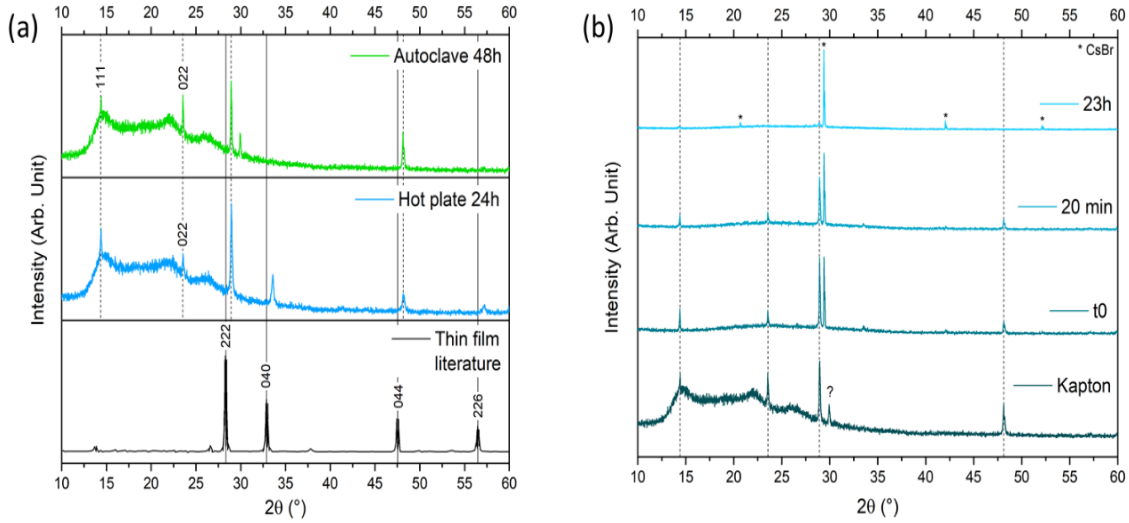

Figure 46. *(a) XRD patterns of Cs_2TiBr_6 films synthesized using the glass container setup (blue) and the autoclave setup (green) on glass protected by Kapton, compared to the reference taken from the literature. (b) Evolution of the Cs_2TiBr_6 XRD spectra when exposed to ambient atmosphere. Vertical solid lines indicate the position of the reference Cs_2TiBr_6 reflections while the dashed lines are the position of the experimentally observed reflections.*

In an attempt to further understand the discrepancies between our experiments and those in literature, we synthesized Cs_2TiBr_6 powder by solid-state and solution-state methods. Impure Cs_2TiBr_6 powder (CsBr impurities) was made by heating $TiBr_4$ and CsBr in a sealed autoclave for 3 days at 200 ˚C. The solution phase synthesis was also carried out in an autoclave by dissolving the binary precursors in HBr, heating to 160 ˚C and cooling over two days to room temperature. Similar to the solid-state synthesis, the resultant powder contained CsBr impurities. Each of these powder samples was unstable under ambient conditions, similar to the thin-films, although the degradation kinetics were slowed, with full transition to CsBr occurring between 24 and 90 hours after exposure.

As the synthesized powders are slightly more stable than the thin films, we were able to carry out diffuse reflectance measurements to extract the bandgap. Figure 47(a) shows the Kubelka-Munk (KM) function modified diffuse reflectance spectra of the Cs_2TiBr_6 powder. All powders exhibit a similar shape in the KM function, with an absorption cut-off at ~600 nm, while Chen et al. observe a cut-off around 650 nm. The extraction of the bandgap leads to similar values for all synthesized powders. The value of the bandgap considering a direct bandgap is 2.0 eV, 0.2 eV larger than the value of 1.8 eV extracted by Chen et al.[31] The difference might arise from the technique used (diffuse reflectance versus UV-vis-NIR spectroscopy) or from the nature of the compound analyzed.

Chen et al. have reported strong photoluminescence (PL) intensity for Cs_2TiBr_6 (Fig. 48(b)), suggesting a low density of defects. We were able to measure the PL on Cs_2TiBr_6 powder synthesized from solution (Fig. 48(a)). Our data suggests a broad peak centered at ~1.8-1.9 eV. However, the signal intensity is very weak and appears quite different from the reported PL. Weak PL emission may suggest a high density of defects or an indirect bandgap, both being detrimental for solar cells. It is also possible that the low PL signal derives from scattering effects in the powder.

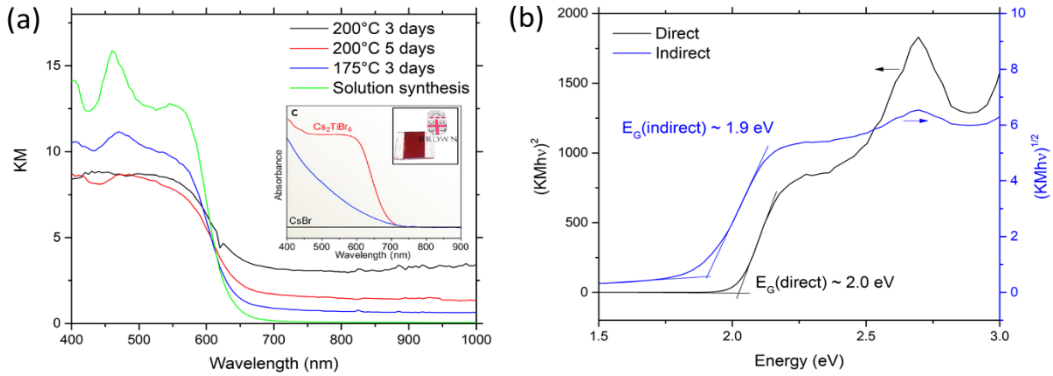

Figure 47. *(a) Diffuse reflectance UV-VIS-NIR spectra of KM function for Cs_2TiBr_6 powders synthesized using solid-state method at different temperatures and duration (black, red and blue) and using solution synthesis. The inset shows the absorption spectra of Cs_2TiBr_6 film obtained after a 12h (blue) and 24h (red) reaction by Chen et al (DOI: 10.1016/j.joule.2018.01.009). (b) Tauc plot considering direct and indirect bandgap for the powders obtained by solution synthesis.*

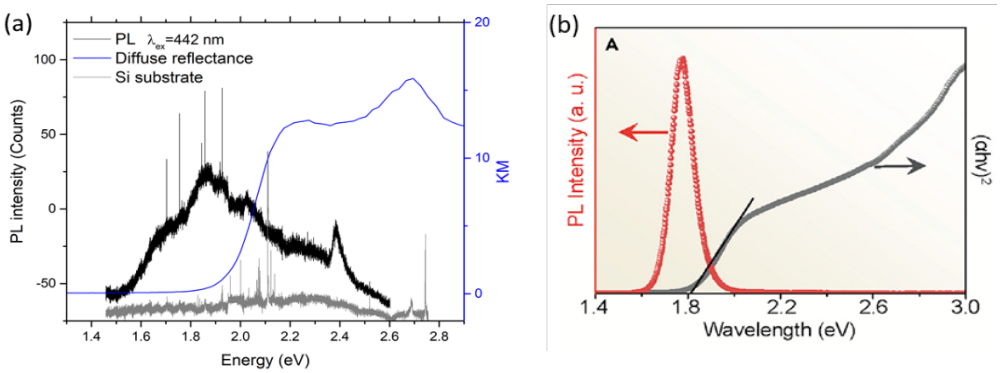

Figure 48. *(a) Photoluminescence and diffuse reflectance spectra for Cs_2TiBr_6 powder synthesized from solution. The photoluminescence of the silicon substrate is provided as a reference. (b) Photoluminescence spectrum and Tauc plot considering a direct bandgap for the Cs_2TiBr_6 thin film published by Chen et al (DOI: 10.1016/j.joule.2018.01.009).*

As a last step to characterize the Cs_2TiBr_6 powder synthesized from solution, we carried out thermogravimetric analysis (TGA). Chen et al. report Cs_2TiBr_6 decomposition starting at 400°C.[31] The TGA analysis on our powder suggests that decomposition starts ~225-290°C, a much lower temperature than reported, but consistent with the volatility of $TiBr_4$.

Our attempt to reproduce the promising Cs_2TiBr_6 results leads to several contradictions with literature results from Chen et al:[31] 1) the XRD peaks are shifted to higher angles suggesting a 0.2 Å smaller unit cell, 2) the films and powders are unstable in ambient atmosphere, 3) absorption spectra suggest a bandgap 0.2 eV larger than reported, 4) a very weak PL emission is measured, and 5) the compound starts to degrade ~225°-290°C instead of 400°C. In order to verify these findings, we received powder samples of Cs_2TiBr_6 from the Padture group who originally published the promising Cs_2TiBr_6. We conducted the same property evaluation and found its properties to match well with the properties of our synthesized powder, in contradiction to the published report.

In summary, we explored different processing techniques to reproduce the Cs_2TiBr_6 thin film and powder results reported.[31] All techniques lead to similar conclusions in

contradiction with the published results. We are also exploring writing a joint paper on the findings of these studies.

Cs(Ge/Sn)I_3 thin-films and stability: In 2018 and 2019, $CsGe_{0.5}Sn_{0.5}I_3$ was identified as a promising Pb-free perovskite material due to its enhanced stability over $CsGeI_3$ and $CsSnI_3$ and the ability to deposit device-quality $CsGe_{0.5}Sn_{0.5}I_3$ thin-films and fabricate >7% efficient solar cells.[4] In contrast to the reported process, we have pursued a solution-based thin-film deposition approach.

Initially, we deposited films using a spin-coating method. We dissolved CsI, SnI_2, and $CsGeI_3$ reactants in a standard DMF or DMSO/DMF mixture and deposited the films directly without using an anti-solvent step. By this method, we were able to successfully deposit films of both $CsSnI_3$ and $CsGe_{0.5}Sn_{0.5}I_3$ (Fig. 49). From comparison to the reference XRD patterns, it can be seen that the $CsGe_{0.5}Sn_{0.5}I_3$ phase occupies a space between the structures of $CsGeI_3$ and $CsSnI_3$ (Fig. 49(a)). The SEM images demonstrate that moving from a pure DMF solution to a DMSO/DMF mixture greatly improves the quality of both the $CsSnI_3$ and $CsGe_{0.5}Sn_{0.5}I_3$ thin films, but the films still tended to have large densities of pin-holes, which is not ideal for inclusion in devices (Fig. 49(b, c)).

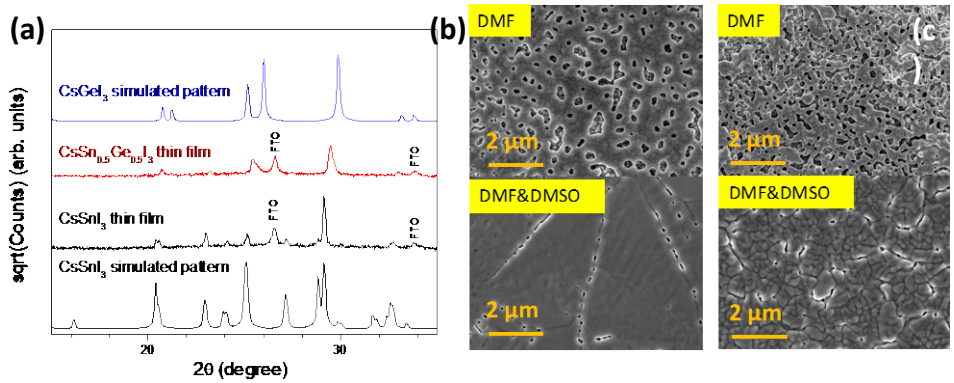

***Figure 49**. X-ray diffraction patterns of $CsSnI_3$ and $CsGe_{0.5}Sn_{0.5}I_3$ thin-films deposited on FTO substrates (a), and SEM images of $CsSnI_3$ (b) and $CsGe_{0.5}Sn_{0.5}I_3$ (c) thin-films deposited from DMF and DMF/DMSO solutions.*

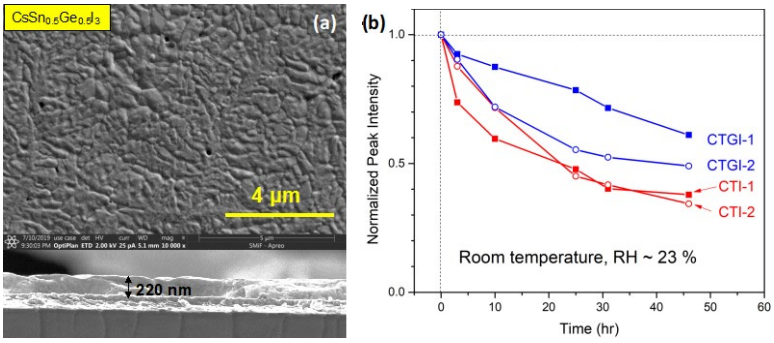

***Figure 50.** (a) SEM images of $CsGe_{0.5}Sn_{0.5}I_3$ films with SnF_2 and $EDAI_2$ and (b) change in main peak intensities of $CsGe_{0.5}Sn_{0.5}I_3$ with $EDAI_2$ additives (CTGI-1) pyrazine (CTGI-2) and $CsSnI_3$ (CTI) films.*

To improve the $CsGe_{0.5}Sn_{0.5}I_3$ film morphology, we explored inorganic and organic solution additives. SnF_2 additive into the DMF/DMSO solution drastically increased the film crystallinity. We also added pyrazine and/or $EDAI_2$ (EDA = ethylene diamine) and found that these additives can reduce the film pinhole density (Fig. 50(a)). These additives can also improve the film stability after exposure to ambient conditions. In particular,

$EDAI_2$-included films tend to be more stable than those containing pyrazine (Fig. 50(b)). These results continue to show the promise of $CsGe_{0.5}Sn_{0.5}I_3$ and work is ongoing to include these films in solar cells with typically perovskite architectures.

Task 17: Final optimization of non-Pb or reduced-Pb perovskite solar cell

There was no research activity under this Task as no Pb-free or Pb-reduced semiconductors proved to be capable of sustaining high performing solar cells at this time.

Conclusions: Overall, this project has greatly furthered the understanding of Pb-based and Pb-free perovskite semiconductors from both theoretical/experimental points of view. The nearly 30 publications that have arisen from this project have and will continue to impact the perovskite community. Within the project, the majority of milestones were met with the exception of those pertaining to the achievement of high-performance non Pb-based perovskite materials.

Computationally, this project has made major advances in the understanding and implementation of theoretical calculations of the formational probabilities and optoelectronic properties of hybrid and inorganic perovskite materials. In particular, the fundamental studies on various perovskite materials have led to intriguing insights into the nature of perovskites with regard to the connection between structural and electronic dimensionality and the nature of band-to-band transitions in these materials.

Experimentally, the researchers advanced the perovskite community's knowledge of Pb-free perovskite materials and device strategies to improve or stabilize Pb-based perovskites. Namely, the project made advances in Pb-free halide (double) perovskites (e.g. $Cs_3Sb_2I_9$, Cs_2SnI_6, tuning of $Cs_2AgBiBr_6$), chalcohalide perovskites, and chalcogenide perovskites (e.g. $BaZr_{1-x}Ti_xS_3$). Additionally, the researchers developed thin-film deposition methodologies for promising non-perovskite InI and silver bismuth iodide. For Pb-based devices, this project has made advances in treatments of perovskite thin films (with SCN) and developed two inorganic contact materials $CuCrO_2$ and NiO_x.

Future work will continue to pursue new, promising Pb-free perovskites, specifically Cs-based Sn and Ge halides.

Budget and Schedule:

The cost shared portion of the budget has been spent according to plan. Deviations from the spend plan for the federal share:

1) **Salaries**: GS working on project received a Duke Fellowship in years 3-4 therefore, the remaining funds were re- allocated towards Materials/Supplies and Other Expenses categories
2) **Consultant Costs**: no longer needed, as the work has been performed by Duke personnel and the funds re-directed towards Materials/Supplies and Other Expenses categories
3) **Tuition Remission**: no longer needed due to GS Fellowship in years 3-4 and funds re-directed towards Materials/Supplies and Other Expenses categories

4) **Travel:** underspent with the remaining balance re-directed towards Materials/Supplies and Other Expenses categories
5) **Material/Supplies and Other Expenses:** overspent with funds provided from underspent categories listed above

A no-cost extension for 1 year enabled continued work and resulted from savings primarily due to fellowships (Wiley Dunlap-Shohl received a Fitzpatrick Fellowship from Duke and Bayrammurad Saparov received a DOE Sunshot Postdoctoral Fellowship).

Path Forward:

Theoretical and experimental work will continue to pursue the lofty goal of achieving a high-performance Pb-free perovskite solar cell. Specifically, work will continue on thin-film deposition of Cs-based Ge/Sn iodides and solid-state synthesis of halide double perovskites and chalcogenide perovskites.

Publications Resulting from This Work:

A. B. Saparov, F. Hong, H.-S. Duan, W. Meng, Y. Yan, & D. B. Mitzi, Thin-film Preparation and Characterization of $Cs_3Sb_2I_9$: A Lead-Free Layered Perovskite Semiconductor, *Chemistry of Materials* **2015**, *27*(16), 5622-5632.

B. W. Meng, B. Saparov, F. Hong, J. Wang, D. B. Mitzi, & Y. Yan, Alloying and Defect Control within Chalcogenide Perovskites for Optimized Photovoltaic Application, *Chemistry of Materials* **2016**, *28*(3), 821-829.

C. F. Hong, B. Saparov, W. Meng, Z. Xiao, D. B. Mitzi, & Y. Yan, Viability of Lead-Free Perovskites with Mixed Chalcogen and Halogen Anions for Photovoltaic Applications, *J. Phys. Chem. C* **2016**, *120*(12), 6435-6441.

D. B. Saparov & D. B. Mitzi, Organic-Inorganic Perovskites: Structural Versatility for Functional Materials Design, *Chemical Reviews* **2016**, *116*(7), 4558-4596.

E. Z. Xiao, W. Meng, B. Saparov, H.-S. Duan, C. Wang, C. Feng, W. Liao, D. Zhao, J. Wang, D. B. Mitzi, & Y. Yan, Photovoltaic Properties of Two-Dimensional $(CH_3NH_3)_2Pb(SCN)_2I_2$ Perovskite: A Combined Experimental and Density-Functional Theory Study, *J. Phys. Chem. Lett.* **2016**, *7*(7), 1213-1218.

F. W. Ke, C. Xiao, C. Wang, B. Saparov, H.-S. Duan, D. Zhao, Z. Xiao, W. Liao, W. Meng, A. J. Cimaroli, C.-S. Jiang, K. Zhu, M. Al-Jassim, G. Fang, D. B. Mitzi, & Y. Yan, Employing Lead Thiocyanate additive to Reduce Hysteresis and Boost Fill Factor of Planar Perovskite Solar Cells, *Advanced Materials* **2016**, *28*(26), 5214-5221.

G. B. Saparov, J.-P. Sun, W. Meng, Z. Xiao, H.-S. Duan, O. Gunawan, D. Shin, I. G. Hill, Y. Yan, & D. B. Mitzi, Thin-film deposition and characterization of a Sn-deficient perovskite derivative Cs_2SnI_6, *Chemistry of Materials* **2016**, *28*(7), 2315-2322.

H. W. Dunlap-Shohl, R. Younts, B. R. Gautam, K. Gundogdu, & D. B. Mitzi, Effects of Cd Diffusion and Doping in High-Performance Perovskite Solar Cells Using CdS as Electron Transport Layer, *J. Phys. Chem. C* **2016**, *120*(30), 16437-16445.

I. Z. Xiao, W. Meng, J. Wang, & Y. Yan, Thermodynamic Stability and Defect Chemistry of Lead-Free Double Perovskite $Cs_2AgBiBr_6$, *Chem Sus Chem* **2016**, *9*(18), 2628-2633.

J. Z. Xiao, W. Meng, D. B. Mitzi, & Y. Yan, Crystal Structure of "$AgBi_2I_7$" Thin Films, *J. Phys. Chem. Lett.* **2016**, *7*(19), 3903-3907.

K. Z. Xiao, W. Meng, D. B. Mitzi, & Y. Yan, Search for Promising New Perovskite-Based Photovoltaic Absorbers: The Importance of Electronic Dimensionality, *Materials Horizons* **2017**, *4*(2), 206-216.

L. Z. Xiao, K. Du, W. Meng, J. Wang, D. B. Mitzi, & Y. Yan, Intrinsic Instability of $Cs_2In(I)M(III)X_6$ (M = Bi, Sb; X = halogen) Double Perovskites: A Combined Density Functional Theory and Experimental Study, *J. Am. Chem. Soc.* **2017**, *139*(17), 6054-6057.

M. W. Meng, X. Wang, Z. Xiao, J. Wang, D. B. Mitzi, & Y. Yan, Parity-Forbidden Transition as an Origin of the Large Optical Bandgap of $Cs_2AgInCl_6$ Lead-Free Halide Double Perovskite, *arXiv preprint* **2017**, arXiv: 1702.03593.

N. W. Meng, X. Wang, Z. Xiao, J. Wang, D. B. Mitzi, & Y. Yan, Parity-Forbidden Transitions and Their Impacts on the Optical Absorption Properties of Lead-Free Metal Halide Perovskites and Double Perovskites, *J. Phys. Chem. Lett.* **2017**, *8*(13), 2999-3007.

O. K. Du, W. Meng, X. Wang, Y. Yan, & D. B. Mitzi, Bandgap Engineering of Lead-Free Double Perovskite $Cs_2AgBiBr_6$ through Trivalent Metal Alloying, *Angewandte Chemie* **2017**, *56*(28), 8158-8162.

P. Z. Xiao, K.-Z. Du, W. Meng, D. B. Mitzi, & Y. Yan, Chemical Origin of the Stability Difference between Cu(I)- and Ag(I)-Based Halide Double Perovskites, *Angewandte Chemie* **2017**, *56*(40), 12275-12279.

Q. X. Wang, W. Meng, & Y. Yan, Electronic Band Structures and Excitonic Properties of Delafossites: A GW-BSE study, *J. Appl. Physics* **2017**, *122*(8), 85104.

R. K. Du, X. Wang, Q. Han, Y. Yan, & D. B. Mitzi, Heterovalent B-Site Co-Alloying Approach for Halide Perovskite Bandgap Engineering, *ACS Energy Lett.* **2017**, *2*(10), 2486-2490.

S. X. Wang, W. Meng, Z. Xiao, J. Wang, D. B. Mitzi, & Y. Yan, First-Principles Understanding of the Electronic Band Structure of Copper-Antimony Halide Perovskite: The Effect of Magnetic Ordering, *arXiv preprint* **2017**, arXiv: 1707.09539.

T. Z. Xiao & Y. Yan, Progress in Theoretical Study of Metal Halide Perovskite Solar Materials, *Adv. Energy Mater.* **2017**, *7*(22), 1701136.

U. Z. Xiao, Y. Yan, H. Hosono, & T. Kamiya, Roles of Pseudo-Closed s2 Orbitals for Different Intrinsic Hole Generation between Tl–Bi and In–Bi Bromide Double Perovskites, *J. Phys. Chem. Lett.* **2018**, *9*(1), 258-262.

V. W. A. Dunlap-Shohl, T. B. Daunis, X. Wang, J. Wang, B. Zhang, D. Barrera, Y. Yan, J. W. P. Hsu, D. B. Mitzi, Room-Temperature Fabrication of a Delafossite $CuCrO_2$ Hole Transport Layer for Perovskite Solar Cells, *J. Mater. Chem. A* **2018**, *6*(2), 469-477.

W. M. Khazaee, K. Sardashti, J.-P. Sun, H. Zhou, C. Clegg, I. G. Hill, J. L. Jones, D. C. Lupascu, & D. B. Mitzi, A Versatile Thin-Film Deposition Method for Multidimensional Semiconducting Bismuth Halides, *Chemistry of Materials* **2018**, *30*(10), 3538-3544.

X. T. Li, X. Wang, Y. Yan, & D. B. Mitzi, Phase Stability and Electronic Structure of Prospective Sb-based Mixed Sulfide and Iodide 3D Perovskite $(CH_3NH_3)SbSI_2$, *J. Phys. Chem. Lett.* **2018**, *9*(14), 3829-3833.

Y. W. A. Dunlap-Shohl, I. G. Hill, Y. Yan, & D. B. Mitzi, Photovoltaic Effect in Indium(I) Iodide Thin Films, *Chemistry of Materials* **2018**, *30*(22), 8226-8232.

Z. M. Khazaee, K. Sardashti, C.-C. Chung, J.-P. Sun, H. Zhou, E. Bergmann, W. A. Dunlap-Shohl, Q. Han, I. G. Hill, J. L. Jones, D. C. Lupascu, D. B. Mitzi, Dual-Source Evaporation of Silver Bismuth Iodide Films for Planar Junction Solar Cells, *J. Mater. Chem. A* **2018**, *7*(5), 2095-2105.

AA. W. A. Dunlap-Shohl, Y. Zhou, N. P. Padture, & D. B. Mitzi, Synthetic Approaches for Halide Perovskite Thin Films, *Chemical Reviews* **2019**, *119*(5), 3193-3295.

BB. D. B. Mitzi, Introduction: Perovskites (special issue), *Chem. Rev.* **2019**, *119*(5), 3033-3035.

CC. Z. Xiao, Z. Song, & Y. Yan, From Lead Halide Perovskites to Lead-Free Metal Halide Perovskites and Perovskite Derivatives, *Advanced Materials* **2019,** 1803792.

DD. B. Zhang, S. Thampy, W. A. Dunlap-Shohl, W. Xu, F.-Y. Cao, C.-C. Tseng, Y.-J. Cheng, D. B. Mitzi, & J. W. P. Hsu, Mg Doped $CuCrO_2$ as Efficient Hole Transport Layers for Organic and Perovskite Solar Cells, *Nanomaterials* **2019**, under review.

Acknowledgment:

This material is based upon work supported by the U.S. Department of Energy's Office of Energy Efficiency and Renewable Energy (EERE) under Solar Energy Technologies Office (SETO) Agreement Number DE-EE0006712.

References:

(1) Yin, W.; Shi, T.; Yan, Y. Unique Properties of Halide Perovskites as Possible Origins of the Superior Solar Cell Performance. *Adv. Mater.* **2014**, *26*, 4653–4658.

(2) NREL. Best Research Cell Efficiencies https://www.nrel.gov/pv/cell-efficiency.html (accessed Apr 1, 2019).

(3) Shao, S.; Liu, J.; Portale, G.; Fang, H.; Blake, G. R.; ten Brink, G. H.; Koster, L. J. A.; Loi, M. A. Highly Reproducible Sn-Based Hybrid Perovskite Solar Cells with 9% Efficiency. *Adv. Energy Mater.* **2017**, *1702019*.

(4) Shen, T.; Ono, L. K.; Ju, M.-G.; Hawash, Z.; Pacifici, D.; Zeng, X. C.; Garces, H. F.; Padture, N. P.; Qi, Y.; Chen, M.; et al. Highly Stable and Efficient All-Inorganic Lead-Free Perovskite Solar Cells with Native-Oxide Passivation. *Nat. Commun.* **2018**, *10* (1), 1–8.

(5) Ran, C.; Wu, Z.; Xi, J.; Yuan, F.; Dong, H.; Lei, T.; He, X.; Hou, X. Construction of Compact Methylammonium Bismuth Iodide Film Promoting Lead-Free Inverted Planar Heterojunction Organohalide Solar Cells with Open-Circuit Voltage over 0.8 V. *J. Phys. Chem. Lett.* **2017**, *8* (2), 394–400.

(6) Harikesh, P. C.; Mulmudi, H. K.; Ghosh, B.; Goh, T. W.; Teng, Y. T.; Thirumal, K.; Lockrey, M.; Weber, K.; Koh, T. M.; Li, S.; et al. Rb as an Alternative Cation for Templating Inorganic Lead-Free Perovskites for Solution Processed Photovoltaics. *Chem. Mater.* **2016**, *28* (20), 7496–7504.

(7) Park, B. W.; Philippe, B.; Zhang, X.; Rensmo, H.; Boschloo, G.; Johansson, E. M. J. Bismuth Based Hybrid Perovskites A3Bi2I9 (A: Methylammonium or Cesium) for Solar Cell Application. *Adv. Mater.* **2015**, *27* (43), 6806–6813.

(8) Jiang, F.; Yang, D.; Jiang, Y.; Liu, T.; Zhao, X.; Ming, Y.; Luo, B.; Qin, F.; Fan, J.; Han, H.; et al. Chlorine-Incorporation-Induced Formation of the Layered Phase for Antimony-Based Lead-Free Perovskite Solar Cells. *J. Am. Chem. Soc.* **2018**, *140* (3), 1019–1027.

(9) Greul, E.; Petrus, M. L.; Binek, A.; Docampo, P.; Bein, T. Highly Stable, Phase Pure Cs2AgBiBr6 Double Perovskite Thin Films for Optoelectronic Applications. *J. Mater. Chem. A* **2017**, *5* (37), 19972–19981.

(10) Jena, A. K.; Kulkarni, A.; Miyasaka, T. Halide Perovskite Photovoltaics:

Background, Status, and Future Prospects. *Chem. Rev.* **2019**, *119*, 3036–3103.

(11) Gross, N.; Sun, Y. Y.; Perera, S.; Hui, H.; Wei, X.; Zhang, S.; Zeng, H.; Weinstein, B. A. Stability and Band-Gap Tuning of the Chalcogenide Perovskite $BaZrS_3$ in Raman and Optical Investigations at High Pressures. *Phys. Rev. Appl.* **2017**, *8* (4), 1–10.

(12) Perera, S.; Hui, H.; Zhao, C.; Xue, H.; Sun, F.; Deng, C.; Gross, N.; Milleville, C.; Xu, X.; Watson, D. F.; et al. Chalcogenide Perovskites - an Emerging Class of Ionic Semiconductors. *Nano Energy* **2016**, *22*, 129–135.

(13) Sun, Y.-Y.; Agiorgousis, M. L.; Zhang, P.; Zhang, S. B. Chalcogenide Perovskites for Photovoltaics. *Nano Lett.* **2015**, *15* (1), 581–585.

(14) Sun, Q.; Chen, H.; Yin, W.-J. Do Chalcogenide Double Perovskites Work as Solar Cell Absorbers: A First-Principles Study. *Chem. Mater.* **2018**, *31*, 244–250.

(15) Pai, N.; Lu, J.; Gengenbach, T. R.; Seeber, A.; Chesman, A. S. R.; Jiang, L.; Senevirathna, D. C.; Andrews, P. C.; Bach, U.; Cheng, Y. B.; et al. Silver Bismuth Sulfoiodide Solar Cells: Tuning Optoelectronic Properties by Sulfide Modification for Enhanced Photovoltaic Performance. *Adv. Energy Mater.* **2019**, *9* (5), 1–11.

(16) Nie, R.; Mehta, A.; Park, B.; Kwon, H.-W.; Im, J.; Seok, S. Il. Mixed Sulfur and Iodide-Based Lead-Free Perovskite Solar Cells. *J. Am. Chem. Soc.* **2018**, *140*, 872–875.

(17) Turkevych, I.; Kazaoui, S.; Ito, E.; Urano, T.; Yamada, K.; Tomiyasu, H.; Yamagishi, H.; Kondo, M.; Aramaki, S. Photovoltaic Rudorffites: Lead-Free Silver Bismuth Halides Alternative to Hybrid Lead Halide Perovskites. *ChemSusChem* **2017**, *10* (19), 3754–3759.

(18) Grätzel, M.; Han, L.; Chen, W.; Wu, Y.; Yue, Y.; Liu, J.; Zhang, W.; Yang, X.; Chen, H.; Bi, E.; et al. Efficient and Stable Large-Area Perovskite Solar Cells with Inorganic Charge Extraction Layers. *Science (80-.).* **2015**, *350*, 944–948.

(19) Sun, W.; Li, Y.; Ye, S.; Rao, H.; Yan, W.; Peng, H.; Li, Y.; Liu, Z.; Wang, S.; Chen, Z.; et al. High-Performance Inverted Planar Heterojunction Perovskite Solar Cells Based on a Solution-Processed CuO x Hole Transport Layer. *Nanoscale* **2016**, *8* (20), 10806–10813.

(20) Sun, W.; Ye, S.; Rao, H.; Li, Y.; Liu, Z.; Xiao, L.; Chen, Z.; Bian, Z.; Huang, C. Room-Temperature and Solution-Processed Copper Iodide as Hole Transport Layer for Inverted Planar Perovskite Solar Cells. *Nanoscale* **2016**, *8*, 15954–15960.

(21) Sun, H.; Hou, X.; Wei, Q.; Liu, H.; Yang, K.; Wang, W.; An, Q.; Rong, Y. Low-Temperature Solution-Processed p-Type Vanadium Oxide for Perovskite Solar Cells. *Chem. Commun.* **2016**, *52* (52), 8099–8102.

(22) Shalan, A. E.; Oshikiri, T.; Narra, S.; Elshanawany, M. M.; Ueno, K.; Wu, H. P.; Nakamura, K.; Shi, X.; Diau, E. W. G.; Misawa, H. Cobalt Oxide (CoO_x) as an Efficient Hole-Extracting Layer for High-Performance Inverted Planar Perovskite Solar Cells. *ACS Appl. Mater. Interfaces* **2016**, *8* (49), 33592–33600.

(23) Tseng, Z. L.; Chen, L. C.; Chiang, C. H.; Chang, S. H.; Chen, C. C.; Wu, C. G. Efficient Inverted-Type Perovskite Solar Cells Using UV-Ozone Treated MoO_x and WO_x as Hole Transporting Layers. *Sol. Energy* **2016**, *139*, 484–488.

(24) Zhang, H.; Wang, H.; Chen, W.; Jen, A. K. Y. $CuGaO_2$: A Promising Inorganic Hole-Transporting Material for Highly Efficient and Stable Perovskite Solar Cells. *Adv. Mater.* **2017**, *29* (8).

(25) Clark, L.; Oró-Solé, J.; Knight, K. S.; Fuertes, A.; Attfield, J. P. Thermally Robust Anion-Chain Order in Oxynitride Perovskites. *Chem. Mater.* **2013**, *25* (24), 5004–5011.

(26) Yu, Y.; Wang, C.; Grice, C. R.; Shrestha, N.; Chen, J.; Zhao, D.; Liao, W.; Cimaroli, A. J.; Roland, P. J.; Ellingson, R. J.; et al. Improving the Performance of Formamidinium and Cesium Lead Triiodide Perovskite Solar Cells Using Lead Thiocyanate Additives. *ChemSusChem* **2016**, *9* (23), 3288–3297.

(27) Jiang, Q.; Rebollar, D.; Gong, J.; Piacentino, E. L.; Zheng, C.; Xu, T. Pseudohalide-Induced Moisture Tolerance in Perovskite $CH_3NH_3Pb(SCN)_2I$ Thin Films. *Angew. Chemie - Int. Ed.* **2015**, *54* (26), 7617–7620.

(28) Ganose, A. M.; Savory, C. N.; Scanlon, D. O. $(CH_3NH_3)_2Pb(SCN)_2I_2$: A More Stable Structural Motif for Hybrid Halide Photovoltaics? *J. Phys. Chem. Lett.* **2015**, *6* (22), 4594–4598.

(29) Vargas, B.; Ramos, E.; Pérez-Gutiérrez, E.; Alonso, J. C.; Solis-Ibarra, D. A Direct Bandgap Copper-Antimony Halide Perovskite. *J. Am. Chem. Soc.* **2017**, *139* (27), 9116–9119.

(30) Biswas, K.; Du, M. H. First Principles Study of Native Defects in InI. *J. Appl. Phys.* **2011**, *109* (11).

(31) Chen, M.; Ju, M.-G.; Carl, A. D.; Zong, Y.; Grimm, R. L.; Gu, J.; Zeng, X. C.; Zhou, Y.; Padture, N. P. Cesium Titanium(IV) Bromide Thin Films Based Stable Lead-Free Perovskite Solar Cells. *Joule* **2018**, *2*, 558–570.

(32) Ju, M. G.; Chen, M.; Zhou, Y.; Garces, H. F.; Dai, J.; Ma, L.; Padture, N. P.; Zeng, X. C. Earth-Abundant Nontoxic Titanium(IV)-Based Vacancy-Ordered Double Perovskite Halides with Tunable 1.0 to 1.8 EV Bandgaps for Photovoltaic Applications. *ACS Energy Lett.* **2018**, *3* (2), 297–304.